May 2015

Optical Cryoimaging of Tissue Metabolism in Renal Injuries: Rodent Model

Fahimeh Salehporchadgani
University of Wisconsin-Milwaukee

Recommended Citation

Salehporchadgani, Fahimeh, "Optical Cryoimaging of Tissue Metabolism in Renal Injuries: Rodent Model" (2015). *Theses and Dissertations*. 961.
https://dc.uwm.edu/etd/961

OPTICAL CRYOIMAGING OF TISSUE METABOLISM IN RENAL INJURIES: RODENT MODEL

by

Fahimeh Salehpour Chadgani

A Thesis Submitted in

Partial Fulfillment of the

Requirements for the Degree of

Master of Science

in Engineering

at

The University of Wisconsin-Milwaukee

May 2015

ABSTRACT

Optical Cryoimaging of Tissue Metabolism in Renal Injuries: Rodent Model

by

Fahimeh Salehpour Chadgani

The University of Wisconsin-Milwaukee, 2015
Under the Supervision of Professor Mahsa Ranji

Injured tissues are often accompanied by morphological or biochemical changes that can be detected optically. Therefore, it would be valuable to visualize the changes in both structure and biochemistry responses of organs for early detection of disease and monitoring of its progression. Oxidative stress is a biochemical byproduct of these diseases. Thus, obtaining sensitive and specific measurements of oxidative stress at the cellular level would provide vital information for understanding the pathogenesis of a disease.

The objective of this research was to use a fluorescence optical imaging technique in order to evaluate the cellular redox state in kidney tissues, and develop an instrument to acquire high resolution 3D images of tissue.

I have improved upon a custom-designed device called a cryoimager to acquire autofluorescent mitochondrial metabolic coenzyme (NADH, FAD) signals. The ratio of these fluorophores, referred to as the mitochondrial redox ratio (RR = NADH/ FAD), can

be used as a quantitative metabolic marker of tissue. The improvement to the instrument includes addition of higher resolution imaging capabilities to the system. This improvement in the resolution of image acquisition enables microscopy imaging in cryo temperatures to obtain high resolution 3D images. The imaging is performed in cryogenic temperatures to increase the quantum yield of the fluorophores for a higher signal to noise ratio. I also implemented an automated tissue boundary detection algorithm. The algorithm will help provide more accurate results by removing the background of low contrast images.

I examined the redox states of kidneys from genetically modified salt sensitive rats (SSBN13, SSp67phx -/-, and SSNox4-/-), in order to study the contribution of chromosome 13, the p67phox gene and the Nox4 gene in the development of salt sensitive hypertension. The result showed that the genetically manipulated rats are more resistant to hypertension caused by excess dietary salt ,, in comparison with salt sensitive (SS) rats.

I also studied how endoglin genes affected the redox state and vascular networks of mice kidneys using high resolution images. The results showed that the next generation of the cryoimager can simultaneously monitor the structural changes and physiological state of tissue to quantify the effect of injuries.

In conclusion, the combination of high resolution optical instrumentation and image processing tools provides quantitative physiological and structural information of diseased tissue due to oxidative stress.

ACKNOWLEDGMENTS

First, I would like to thank my graduate advisor Dr. Mahsa Ranji for her assistance and support of this project. I would not be where I am today if it were not for her guidance and input. Her standards of excellence and commitment to her students have truly been an inspiration. Under her tutelage, I have learned and grown as both a researcher and a person; I am truly grateful for the opportunity to study and learn from her.

Most of the results described in this thesis would not have been obtained without a close collaboration with few laboratories. I would like to thank Dr. Cowley, Medical college of Wisconsin, and Dr. Sheibani from UW-Madison, which have provided me with the tissue samples covered in this research and his guidance in the biological side of the research was also invaluable to me.

I would like to sincerely acknowledge my friends and lab mates in the Biophotonics Lab for their kindness and moral support during my study. I am most grateful to Zahra Ghanian, Jeffry Sugar and Reyhaneh Sepehr, whose endless help and supports made this research possible and the research life a pleasant.

Lastly and most importantly, my deepest gratitude goes to my family for their love and support. My husband, Hamed, who has always supported, encouraged and believed in me throughout my life. My parents who always inspired me with hope and faith.

Thank you all.

TABLE OF CONTENTS

LIST OF FIGURES

LIST OF ABBREVIATIONS

ADP - Adenosine Diphosphate

ATP - Adenosine Triphosphate

CCD - Charged Coupled Device

ETC - Electron Transport Chain

Eng - Endoglin gene

$FADH_2$ - Flavin Adenine Dinucleotide

FOV - Field Of View

HHT-1 - Hereditary Hemorrhagic Telangiectasia

NADH - Nicotinamide Adenine Dinucleotide

NAD(P)H - Nicotinamide Adenine Dinucleotide Phosphate

OS - Oxidative Stress

RR - Redox Ratio

UV - Ultraviolet

ROS - Reactive Oxygen Species

LN_2 - Liquid Nitrogen

LP/mm - Line Per millimeter

PVA - polyvinyl Alcohol

Chapter 1: Introduction and Background

Overview

Biophotonics is a progressing research area involving a combination of biology and photonics, to bring dedicated instruments and rigorous measurement methods in the field of biology utilizing light, one of the most precise tools of nature [1]. Photonics is the science and technology of the generation, propagation, and detection of light [2]. Biophotonics can also be described as a field that deals with the development and application of optical techniques, particularly imaging, to study interactions between biological items and photons [1]. The interaction between light and tissue refers to some optical phenomena such as emission, absorption, reflection, modification, and creation of radiation from biomaterials [3, 4]. One of the most common methods that have been used to gather information about biological organs is the study of fluorescence light emitted from biomaterials. Fluorescence imaging, a technique capable of producing quantitative measures related to the tissue health, has been employed for the analysis of many different sample types in clinical practice and research [5].

Various preclinical and clinical studies have established fluorescence imaging as a suitable technique for medical diagnosis and monitoring due to its simplicity, cost effectiveness, higher level of sensitivity and specificity in comparison with other imaging techniques such as MRI and CT [6].

The aim of the research presented in this thesis is to implement and apply optical tools to monitor metabolic state in diseases of clinically important disorders, such as salt-induced hypertension. The ultimate goal of our research is to translate optical fluorescent imaging to clinics as a reliable tool for spatiotemporal diagnosis of injuries.

1.1 My Contributions

I have contributed to three major areas in this research:

1- Instrumentation:

I have been involved in the modification and implementation of the cryoimager to add high resolution capability to the system. This improvement of the cryoimager enables microscopy imaging in cryogenic temperatures, which allows for visualization of structural changes due to the injury, and correlate the results with metabolic changes in the tissue. I have also contributed to the optimization of the cryoimaging system's microtome hardware to increase the quality of the acquired images.

2- Image processing:

I have processed raw images from the cryoimager to evaluate the redox ratio of frozen tissues. The processing was mostly done via algorithms I developed in Matlab, and ImageJ. In order to improve the accuracy of the quantification and construct clearer 3D- rendered representation images, I have developed an image processing algorithm to automatically detect the tissue's boundary and remove the background surrounding the detected borders. In some cases, such as having low contrast images due to the mounting medium, this algorithm results in the improvement of the data analysis outcome. The algorithm is often used in the processing of high resolution imaging data.

3- Interpretation of metabolic data in renal injuries:

The focus of this thesis is kidney tissue metabolism in different renal injuries. The first injury model studied was salt sensitive hypertension. Hypertension is a major cause in the development of diseases, such as strokes, heart failure, and end stage renal injuries

[7]. In the US, almost 31% of adults over the age of 18 are affected by hypertension [8, 9]. Excess dietary salt intake is one of the most important environmental factors in development of salt sensitive hypertension [7, 10]. Because the susceptibility of individuals to salt intake is genetically determined, there exists a need to study the genes that contribute to salt sensitive hypertension [7]. I studied the effect of chromosome 13, the p67phox gene, and the Nox4 gene in the development of salt sensitive hypertension. The results of this study validated the performance of the cryoimaging technique in measuring the oxidative state of the tissues.

The second injury model studied was a severe vascular dysplasia (HHT-1 or Endoglin+/-) with the aim of investigating structural changes in the kidney due to disease as well as the mitochondrial redox state of the tissue with the new cryo-microscopy setup. HHT-1 (Hereditary hemorrhagic telangiectasia) is a good model of a disease in which the vasculature networks of several different organs, such as lung, kidney and brain are affected [11-13].

1.2 Biological Background

1.2.1 Cell structure and the mitochondrion

All known living organisms are composed of cells [14]. Cell is the structural and functional unit of life. A generalized structure of the animal cell is shown in Fig.1-1(a) [15]. Many injuries and illnesses can be traced back to irregularities in the operations within the cell [16]. Although all cellular organelles are essential to the organism’s health and ability to survive, it is the mitochondria that play a central role in cellular energy metabolism (see Fig.1-1(b)) [17, 18]. The number of mitochondria per cells varies depending on the energy requirements; tissues with a high capacity to perform aerobic metabolic functions, such as skeletal muscle or kidneys, will have a larger number of mitochondria [14, 19]. Mitochondria have two membranes within the inner membrane encloses and convolutes into the mitochondrial matrix, forming cristae [20]. A major consequence of the architecture of mitochondria is the impermeability of the inner membrane, which facilitates the generation of a proton gradient [20].

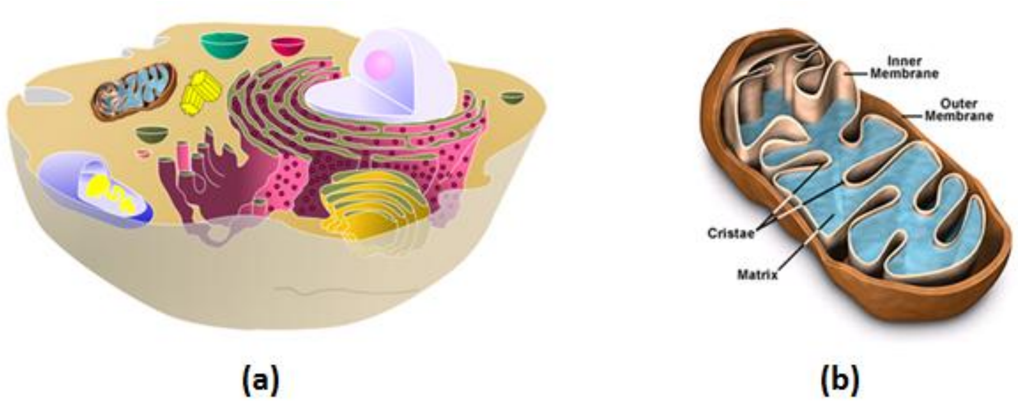

Figure 1-1: (a) Cell structure including its organelles [9], (b) Mitochondrion [18].

1.2.2 Electron transport chain (ETC)

Mitochondria are the powerhouses of the living cell, and it is responsible for producing most of the cell‘s energy through oxidative phosphorylation [21]. This process of energy production requires the proton gradient which is provided by electron trasport chain (ETC), including four major complexes. These components are located in the inner mitochondrial membrane. Fig.1-2 [22] gives a schematic representation of the electron transport chain. Two mitochondrial metabolic coenzymes, NADH and FADH2, are the main electron carriers in the electron transport chain. When electrons are transported along the chain, three of the four complexes (I, III, and IV) act as proton pumps, sending out protons from the matrix and generating the proton gradient. The protons are allowed to return to the matrix through another enzyme, the ATP synthase [19]. This enzyme uses the proton gradient to generate ATP (adenosine triphosphate) from ADP (adenosine diphosphate) and Pi (inorganic phosphate). Therefore, variation in the redox state of NADH and FADH2 can be an indicator of a change in tissue bioenergetics [20, 23].

Britten Chance and colleagues [24] [25] [26] have demonstrated that the autofluorescence signal from tissues originates almost exclusively from NADH in the mitochondria. The contribution of NADH, which is present in the cytosol, is small since as soon as NADH is produced by glycolysis in the cytosol, the electron from NADH is transported to the mitochondria through the malate-aspartate shuttle. NADH is therefore largely oxidized to NAD in the cytosol, consistent with the low NADH/NAD ratio in the cytosol as calculated from the lactate dehydrogenase (LDH) reaction (which is mostly an equilibrium reaction). We are unaware of any evidence showing a significant presence of NADH in the cytosol. Regarding FAD, it is known that FAD is strictly localized within the mitochondria [27, 28] so the FAD signal that we are detecting derives only from the mitochondria [29, 30].

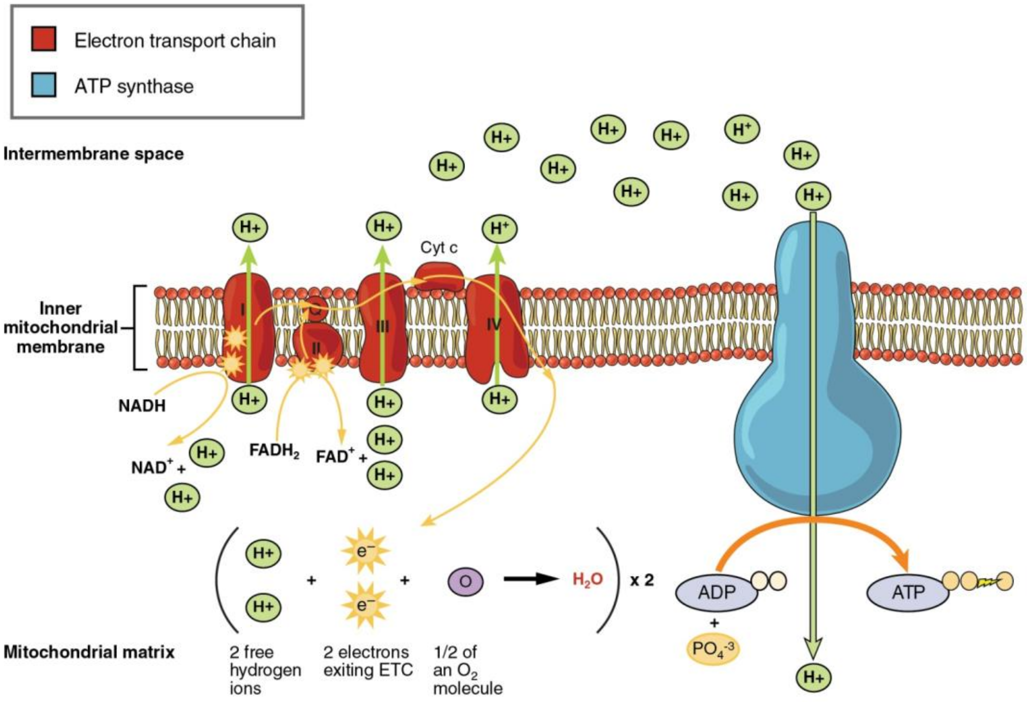

Figure 1-2: Electron Transport Chain. Simplified block diagram of the electron transport chain [22]

1.2.3 Oxidative stress

In normal conditions, the final destination for an electron along the electron transport chain is its reduction to produce water. However, about 0.1–2% of electrons passing through the chain do not complete the whole series and instead leak directly to oxygen, resulting in the generation of the superoxide free-radical ($O_2^{\cdot -}$). Free-radicals are highly reactive molecules that contribute to the production of other oxygen-derived species such as H_2O_2 [31, 32]. These reactive oxygen spices (ROS) play a causal role in the development of cardiovascular disease, including hypertension, diabetes, and heart failure [33]. The term "oxidative stress (OS)" reflects an imbalance between the production of ROS and the ability of a biological system to eliminate the resulting damage, causing an increased level of ROS [34].

Indeed, in many cases the amount of oxygen available to a cell can accurately represent the health of the cell and be used as a tool for diagnosis. In these cases, the oxidation state, or redox state, of the tissue serves as a sensitive and reliable measure for evaluation of cell behavior [35].

1.2.4 NAD(P)H oxidase

The NADPH oxidases (nicotinamide adenine dinucleotide phosphate-oxidases) are transmembrane multi-subunit enzyme complexes whose primary biological function is to produce ROS [36, 37]. The prototypical NADPH oxidase consists of at least six subunits: four cytosolic proteins, Rac, p40phox ("phox" stands for phagocyte oxidase), p47phox and p67phox, together with two membrane-bound components, gp91phox (also termed "Nox2") and p22phox [20, 38, 39]. In unstimulated cells (while cell is at rest), p47phox, p67phox, and p40phox exist in the cytosol, whereas p22phox and gp91phox are in the membrane (see Fig.1-3 (a)) [40]. Once activated, these subunits translocate to the membrane and form an active enzyme (see Fig.1-3 (b)) [40, 41].

Although NAD(P)H oxidases were originally considered enzymes, expressed only in phagocytic cells involved in host defense and innate immunity, recent evidence have demonstrated that similar NADPH oxidases are present in a wide variety of nonphagocyte cells and tissues [20, 42]. These newly discovered homologs, along with gp91phox, are designated the Nox family of NAD(P)H oxidases [43, 44]. The Nox family is comprised of seven members, including Nox1, Nox2 (formerly termed “gp91phox”), Nox3, Nox4, Nox5, Duox1, and Duox2 [40, 45]. Nox4, originally termed “Renox” (renal oxidase), because of its abundance in the kidney, is also found in vascular cells and osteoclasts [46, 47]. The regulation and function of each Nox remains unclear, but it is evident that Nox enzymes are critical for normal biological responses and that they contribute to cardiovascular and renal disease, including hypertension and atherosclerosis [34, 48, 49]. A complete coverage of the biochemistry and physiology of the NADPH oxidase itself is beyond the scope of this thesis. Here we highlight developments in the field of ROS and renal disease, focusing specifically on the protective effect of subunits of NAD(P)H oxidase in hypertension, which are Nox4 and P67phox.

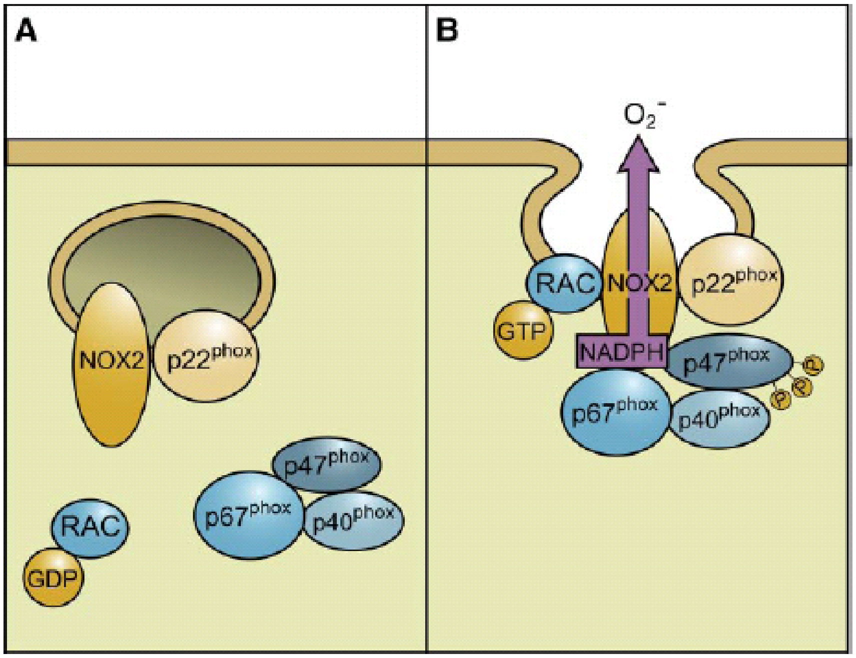

Figure 1-3: Assembly of NADPH oxidase. (a) At rest (b) Active [40].

1.3 Fluorescence imaging

Fluorescence imaging in the past several decades became a promising structural and molecular imaging technique for clinical diagnosis [50, 51]. The optical signals can provide greater insight into biological tissues at the molecular level and are correlated with physiological information about the tissue [52]. Fluorescence imaging as an ideal technique has been widely used to analyze various type of samples including fixed and living specimens, and different organs [53-56]. This method deals with the selective and specific detection of molecules at small concentrations with a good signal-to-noise ratio [57]. As a practical technique, fluorescence imaging has been exploited to examine tissue health and redox state in intact organs. This method is capable of determining the amount of oxygen existent in the cell's environment via the intrinsic fluorescence of some of the chemicals present in the cell [35].

1.3.1 Principle of fluorescence

Fluorescence spectroscopy works based on the phenomenon that certain molecules, referred to as fluorophores, absorb energy of a specific wavelength and then re-emit energy that is detectable as visible light, at a different but equally specific wavelength. The basic principle of fluorescence is shown in a Jablonski diagram Fig.1-4. Electrons of a molecule are generally located in the ground state (S_0). Once a resting molecule is exposed to a source of energy, e.g. a bright light source, it absorbs a photon with the energy $h\nu_{ex}$. The absorption excites the molecule and increases its energy level, the unstable electronic singlet state (S_1') as depicted by the green arrow. This excited state is rather unstable and thus has a very short lifetime. The excited fluorophore falls to the lowest vibrational energy level within the electronic excited state (S_1), dissipating the energy in the form of heat (yellow arrow). Finally, the orbital electron relaxes from the excited state S_1 toward the ground state S_0, while emitting the fluorescence light (red arrow). The energy of the photon that is emitted in this process, $h\nu_{em}$, is exactly the difference between S_1 and S_0. Each fluorophore has a characteristic excitation and emission wavelength, which is determined by the difference in energy between electronic energy levels [53]. The amount of energy emitted and its corresponding wavelength depend on both the fluorophore and the chemical environment of the fluorophore [57].

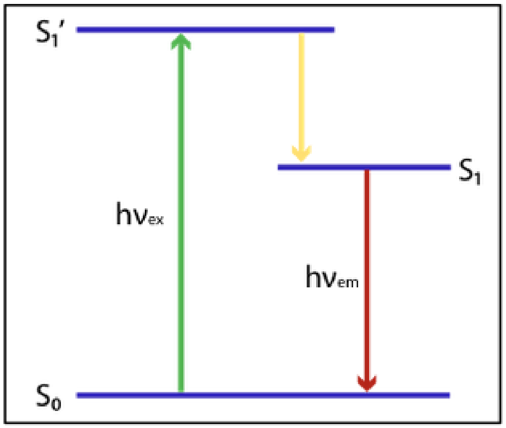

Figure 1-4: Jablonski Diagram of Fluorescence [53].

Based on the conservation of energy law in the system, since the molecule lost some portion of energy as a heat, the emitted light has a lower energy, and therefore longer wavelength compare to the excitation light. This phenomenon is known as ***Stokes shift***, and has been shown in Fig.1-5 [53, 58].

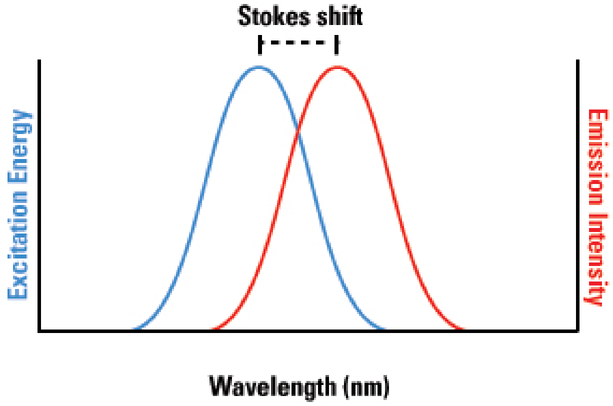

Figure 1-5: Stokes shift [58].

The probability of emitting a fluorescence photons after absorption of excitation photon, termed the fluorescence ***quantum yield***, is the indicator of the efficiency of the fluorescence process. It is defined as the ratio of the number of photons emitted to the number of photons absorbed [53, 58].

1.3.2 Endogenous fluorophores in mitochondria

Fluorescent imaging is associated with the administration of fluorescent probes, which are categorized as endogenous (naturally occurring) or exogenous (external labeling) fluorophores. There are several endogenous fluorophores in tissues and cells that can generate autofluorescence, such as keratin, melanin, NADH and FAD. Two of these fluorophores, NADH (reduced form of NAD^+) and FAD (oxidized form of FADH2), are essential proteins in the metabolic pathway of mitochondria [14]. The fluorescence light of these coenzymes can be monitored by optical detectors and have been exploited to assess the metabolic activity in different tissues [55]. The excitation and emission spectra of these intrinsic fluorophores are presented in Fig.1-6 [59, 60]. Neither their excitation spectra overlap each other nor their emission spectra, which assures the selective detection of fluorescence between the two fluorophores.

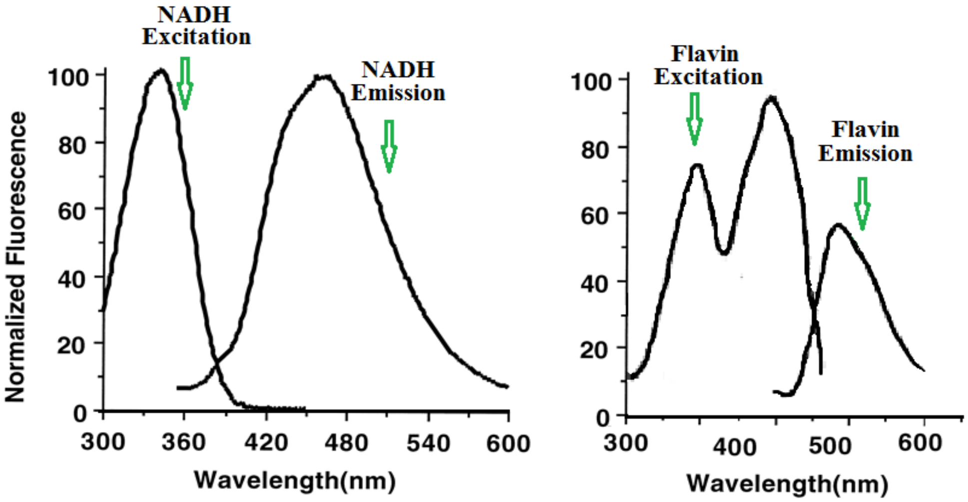

Figure 1-6: NADH and FAD Fluorescence Spectra [50,51].

NADH only fluoresces in its reduced form, and FAD only fluoresces in its oxidized form, so their fluorescence signals have been used as indicators of tissue mitochondrial redox state, in the context of clinical diagnosis [55]. In addition, the ratio of these two fluorophores (NADH/FAD), called the mitochondrial redox ratio (NADH RR), is used to identify the metabolic state within the tissue [26, 56, 61-63].

1.3.3 Relation between ROS and redox ratio (NADH/FAD)

As stated above, the electrons from NADH produced during glycolysis within the cytosolic compartment are quickly transported into the mitochondria through the malate-aspartate shuttle with NAD remaining in the cytosol. Thus, the tissue redox ratio can be effectively considered as the balance between fluxes through the TCA cycle and the ETC. In the presence of oxidative stress, the ETC does not function efficiently due to oxidative damage of ETC complexes. This leads to excess electron leak and ROS production which leads to the accumulation of the mitochondrial coenzymes NADH and FADH2 in their oxidized forms NAD and FAD. Hence, the levels of NADH decrease and the levels of FAD increase resulting in a decreased NADH/FAD redox ratio. Therefore lower tissue redox ratios represent higher levels of oxidative stress and the tissue redox ratio shows an inverse relationship with the oxidative stress level of the tissue.

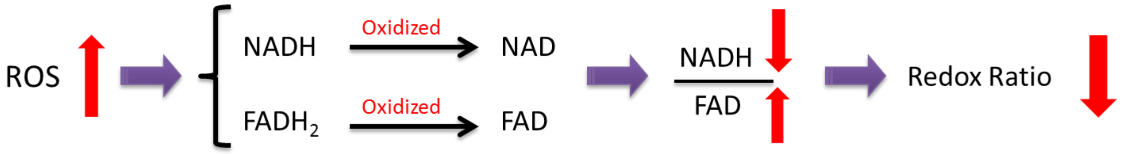

1.4 Animal model of hypertensive kidneys

Hypertension is one of the most influential factors in the development and progression of strokes, heart failure, and end-stage renal disease [7]. The kidneys play a key role in keeping a person's blood pressure in a healthy range, and blood pressure, in turn, can affect the health of the kidneys. High blood pressure, also called hypertension, can damage the kidneys and lead to chronic kidney disease [64]. There is an increasing evidence that suggests excess dietary salt intake has a greater impact on individuals who have a genetic predisposition for salt sensitivity [10]. Therefore, there is a need to investigate ways to protect individuals against developing salt sensitivity [7].

1.4.1 Salt sensitive hypertension

Essential hypertension affects 972 million (26.4%) of the world's adult population and 67 million (31%) of US adults over the age of 18 [8, 9]. There are many different environmental factors that cause hypertension. One of the most important factors is excess salt consumption. Nearly half of the adults with hypertension in the US exhibit enhanced blood pressure sensitivity to dietary salt intake, reaching as high as 75% in African Americans [65-67]. A number of mechanisms are recognized to contribute physiologically to the development of hypertension, with the most prominent of these being the reduced ability of the kidneys to excrete sodium, as characterized by a reduction in the pressure-natriuresis relationship [68, 69].

1.4.2 Mitochondrial dysfunction in hypertension

While ROS play essential roles in normal renal function, oxidative stress is deeply involved in pathological conditions related to abnormal kidney function, including salt-sensitive hypertension and diabetes [20, 33]. It is recognized that an imbalance in the redox state of the kidney contributes importantly to this renal dysfunction. For instance, Dahl salt-sensitive rats exhibit elevated levels of $O^{\bullet}{}_2^-$ and H_2O_2 in both the medulla and cortex, which contribute to reductions of medullary perfusion, reduced sodium excretion, glomerular sclerosis, tubular injury, and interstitial fibrosis [6,26,40,41,42]. It is also known that NADPH oxidase activity is upregulated by prolonged infusion of a high salt diet [70]. Since these are major factors underlying the development of hypertension, renal NADPH oxidase may have an important pathophysiological role [71].

The sources and localization of ROS production within the *kidney* have been of great interest given the need to develop therapeutic strategies that can reduce ROS in the kidney, where it is produced in excess under conditions like aging, diabetes and hypertension. Mitochondria and NADPH-oxidases (Noxs) are major sources of $O^{\bullet}{}_2^-$ and H_2O_2 in the *kidney* [72-75] with the mitochondria appearing to be both a source of ROS production and also a target for ROS produced by NADPH oxidase (referred to as ROS-induced ROS production [76-79]. Of the seven identified Nox isoforms, Nox2 and Nox4 appear to be the two most robustly expressed in the kidney [80], although the specific functions and relative importance of these isoforms remain unclear. More specifically within the renal outer medulla , the source of excess ROS production has been attributed to NADPH-oxidase [7]. There is also an ample evidence that indicates the mitochondria are responsible for most of the fundamental ROS production in the outer medullary region of the kidney [81].

1.4.3 Animal models for salt sensitive hypertension

The Dahl salt-sensitive (SS) rat mimics many of the traits found in African American hypertensive patients [82-84] and has been studied extensively as a model of a complex multifactorial genetic disease [85-89].

A total of four groups of rats (SS, SSBN13, SSNox4-/- and SSp67phox-/-) were studied in this thesis. All the rats were bred and housed in an American Association for Accreditation of Laboratory Animal Care-approved animal care facility at the Medical College of Wisconsin. The rats had free access to food and water throughout the study.

All experimental procedures were approved by the Institutional Care and Use Committee of the Medical College of Wisconsin.

Generation of SSBN13 Consomic Rats:

There are ample evidences shown that a powerful gene, or a set of genes, within chromosome 13 of Brown Norway (BN/Mcw) rats confers protection from the detrimental effects of high salt to the Dahl salt-sensitive (SS/Mcw) rats [90, 91]. The consomic rats (SS.BN13) were bred to investigate the effect of this gene upon the development of salt-sensitive hypertension. In order to produce consomic rats (SS.BN13), chromosome 13 from normotensive inbred Brown Norway rats (BN/Mcw) was introgressed into the background of Dahl salt-sensitive (SS/Mcw) rats were bred [88]. Genotyping has found this strain to be 98% identical to SS rats differing by only the subset of allelic differences (including the renin gene) present on chromosome 13 that were carried from the parental BN strain [81, 90, 92].

p67phox-Null Mutant SS Rat:

To determine the functional relevance of the NADPH-oxidase subunit, p67phox, in the development of salt-sensitive hypertension in SS rats, the SSp67phox null rat (p67phox-/- rat) model was generated as weanlings from colonies maintained at the Medical College of Wisconsin. The SSp67phox null rats were produced in the genomic background of SS rats using zinc-finger nuclease (ZFNs) techniques [93, 94]. Genomic DNA of p67phox-null mutant (p67phox-/-) rats was sequenced. Sequencing results suggested there was a 5 bp deletion (GAGAA) in the genomic sequence of p67phox-/-

rats. The western blot and respiratory burst experiments were performed to validate the generation of p67phox-/- rats. p67phox is known to be critically involved in the respiratory burst of macrophages [95, 96]. The respiratory burst experiments demonstrated a complete loss of functional respiratory burst activity in macrophages obtained from p67phox-/- rats.

Chapter 2: Optical Cryoimaging System

Overview

NADH and FAD co-enzymes in the mitochondria indicate the cellular redox state of an intact organ. Cellular redox state is a quantitative marker to examine oxidative stress of tissue, which assess the oxidation state and health of the tissue. There are a handful of fluorescence imaging methods to probe the biochemical and morphological characteristics of tissues such as microscopic fluorescence imaging. Some of these methods require offline assay analysis on homogenized tissue, and take significant time to analyze. Our cryoimaging has the ability to determine endogenous and exogenous fluorophores relative concentrations with high fluorescence quantum yields. This device uses the autofluorescence of the previously mentioned NADH and FAD co-enzymes within the mitochondria to determine the cellular redox state.

Cryoimaging is capable to construct a 3-D image of a tissue, which becomes important for structural studies of a large biological sample. It also provides a strong fluorescence quantum yield of NADH and FAD as compared to room-temperature imaging techniques. In addition, the cryoimaging evaluates the ratio of NADH and FAD. By evaluating the ratio of these two coenzymes, some of the confounding factors in determining the oxidative state can be removed, such as absorbers, including blood, as well as system variations. This ratio is a quantitative marker of tissue metabolism and is independent of the concentration of the mitochondria in the tissue.

The cryoimager is a custom-designed imaging system, consisting of automated hardware and software to acquire images of up to five fluorophores from the frozen tissue sections. The cryoimaging system consists of a 200W mercury arc lamp light source used to excite fluorophores from tissue and a CCD camera to collect the tissue autofluorescence. Desired wavelengths are selected by filtering the broad band output of the mercury arc lamp. After it has been reflected off a cold mirror, filters are selected to excite the desired fluorophores in the exposed surface of the frozen tissue block. Then the emitted light from tissue is collected by a CCD camera after passing through a band-pass filter to remove undesired lights.

A schematic of a cryoimaging system along with an actual device can be seen in Fig.2-1. In order to construct a 3D image of the tissue a motor-driven blade sequentially slices the frozen tissue with an adjustable thickness.(add a sentence about imaging each slice and combining to form a full 3D image) The tissue temperature is kept at -40 centigrade during the experiment. This helps to preserves the metabolic state of the tissue, and provides higher quantum yields. Further details of each component are found in the following section.

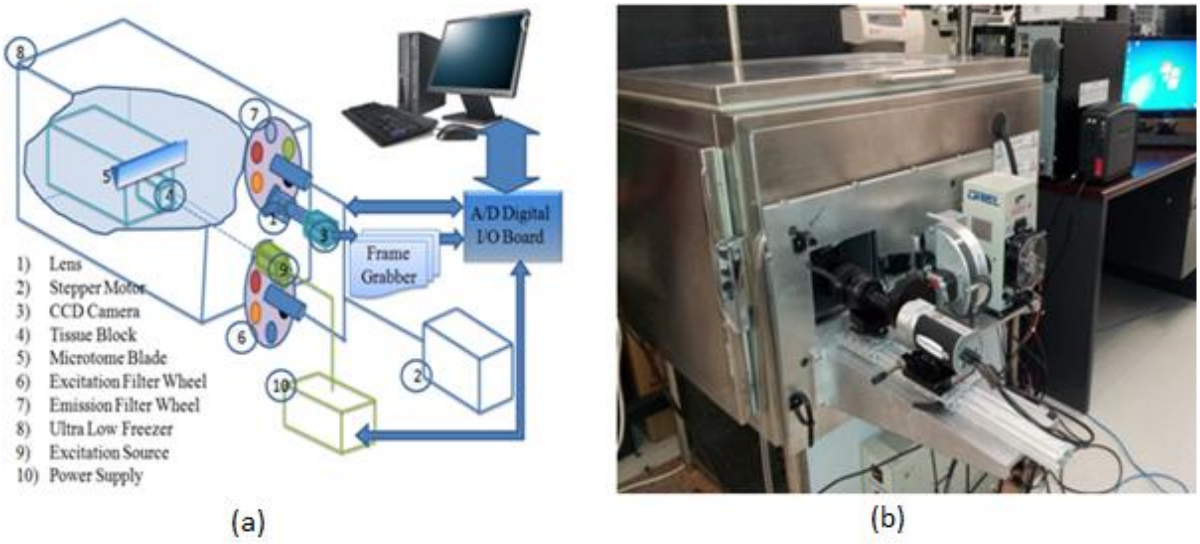

Figure 2-1: (a) Cryoimager schematic. (b) Cryoimager

2.1 Optical system and components

Like other fluorescence imaging systems, the cryoimager possesses an excitation and emission path. All of the optical components making up these paths are located outside of the freezer. In the following sections, an overall view of each path is explained first, then characteristics of all optical components are described.

Excitation light pathway

The excitation light path, which is shown in Fig.2-2, starts with an intense light source. The light source used in the cryoimaging setup is a mercury-arc lamp that emits a broadband light. An initial rough filtering is performed by removing the infrared region of the spectrum utilizing reflection from a cold mirror. The light is then guided through a filter wheel to select the desired wavelengths for excitation of NADH and FAD

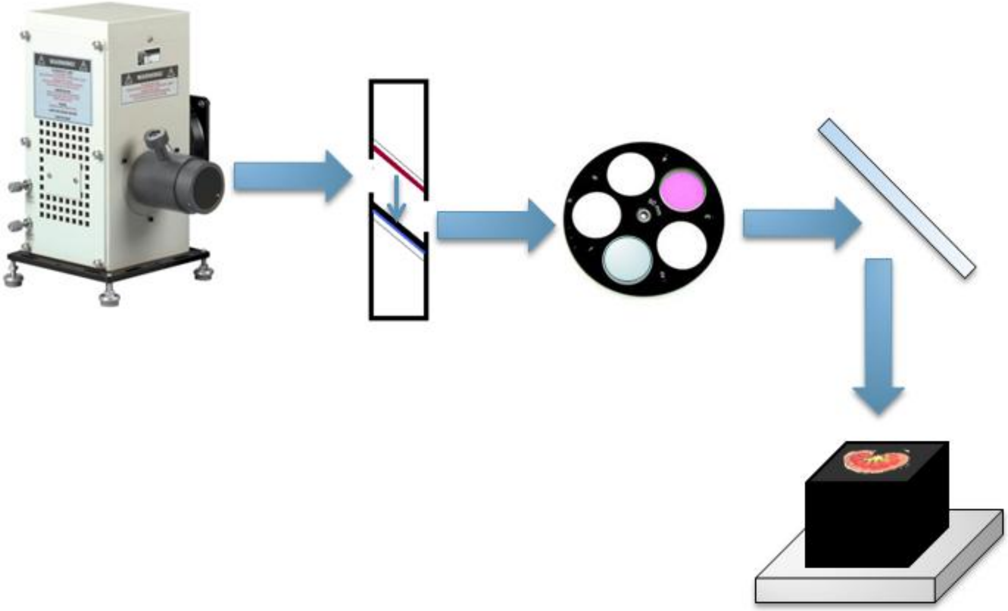

Figure 2-2: Cryoimager excitation path

fluorophores. After passing through the proper filter, the excitation light is incident normally on the tissue surface via reflecting from a mirror. At each slice multiple fluorophores can be excited by rotating the filter wheel.

Emission light pathway

The tissue exposed by the excitation light emits fluorescence light which is delivered to an emission filter wheel. The emission light pathway has been shown in Fig.2-3. By sending emission light through a filter wheel, undesired lights such as reflected and ambient light are blocked. In the next step, filtered light is coupled into a lens to create an image on a CCD camera. The camera records a fluorescence image of the tissue block in desired pixel dimensions to be later analyzed for fluorophore distribution. It should be mentioned that the distance between the tissue surface and the lens, referred to as the working distance, is selected to be24.3 cm, because it provides a field of view large enough to image the whole kidney.

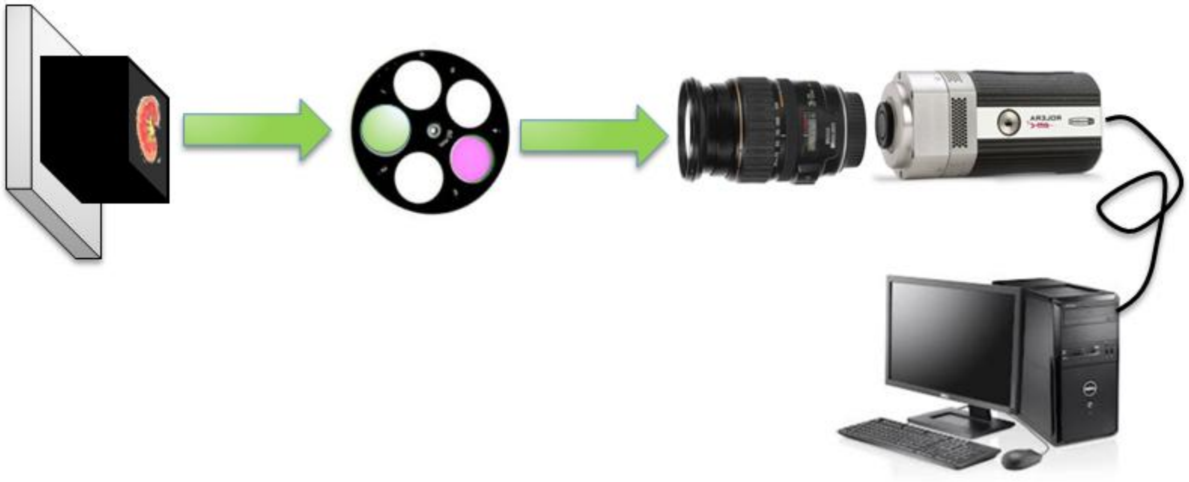

Figure 2-3: Cryoimager emission path

The specifications of the components used in this optical setup are described as follows.

2.1.1 Light source

The illumination source used in the cryoimaging setup is a 200 W mercury-arc lamp (Oriel, Newport Instrument, 6283NS, CT, U.S.A). This is an intense broadband light source, and the most significant feature of its spectrum is the presence of strong spectral peaks corresponding to the excitation wavelengths of both NADH and FAD fluorophores. As can be seen from Fig.2-4, the lamp produces a peak at 365 nm, which falls right on the high end of the NADH excitation spectrum, and another peak at 436 nm, which is at the low end of the FAD excitation spectrum [97]. The white light from the mercury arc lamp is coupled into a condenser to homogenize the output light. The lamp intensity will stabilize at its peak 10 to 15 minutes after turning on the power supply.

The mercury arc lamp has a limited lifetime of 1000 hours and should be replaced when needed.

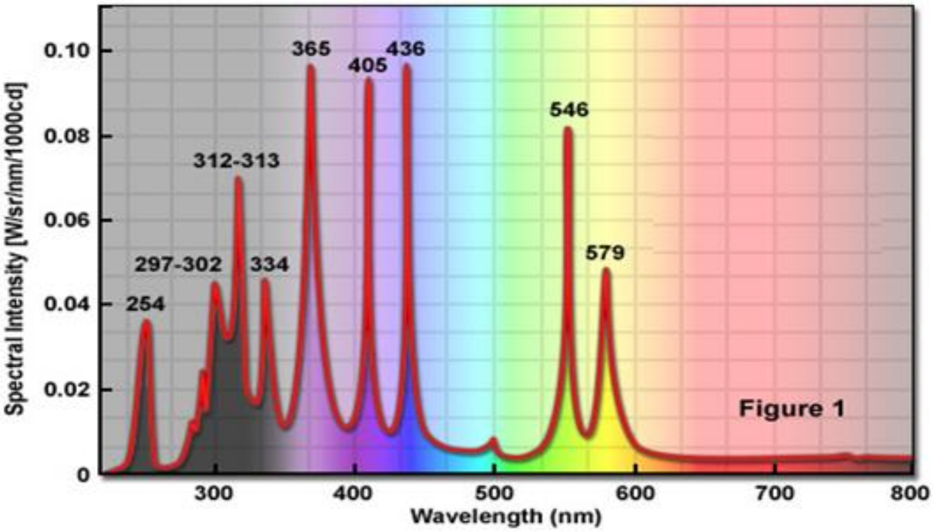

Figure 2-4: Spectral intensity of Mercury arc lamp [87]

2.1.2 Cold mirror

A cold mirror is a specialized dielectric mirror that reflects almost 90% of visible light while very efficiently transmitting infrared wavelengths. The infrared wavelengths are blocked to decrease the undesirable heat caused by infrared radiation on tissue. The cold mirrors are constructed from multi-layer dichroic coating and can be designed for an incidence angle ranging between zero and 45 degrees. A schematic of the cold mirror has been shown in Fig.2-5 [98].

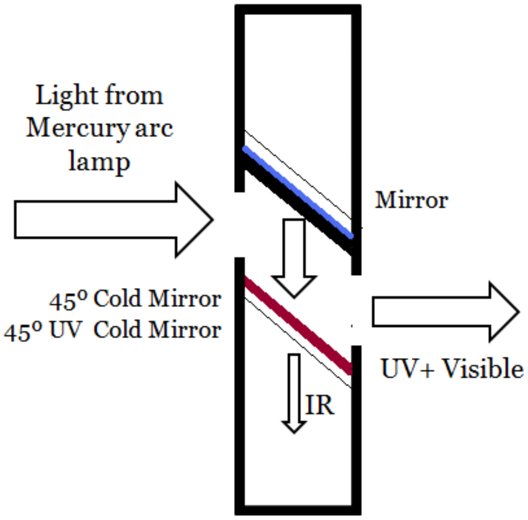

Figure 2-5: Cold Mirror

2.1.3 Motorized optical filter wheels

The cryoimaging system includes two motorized filter wheels to isolate the fluorescence excitation and emission wavelengths. Each unit is designed with five slots of fifty-millimeter diameter to mount optical band-pass or neutral density filters. A controller and a stepper motor (Oriental Motor Vexta Step Motor PK268-01B) rotate the filter wheels to adjust which filters are being used for imaging different fluorophores. The utilized optical bandpass filters allow transmission through a specified range of wavelengths, but has an optical density of 5 for wavelengths outside of a very narrow transition regime. Specification of the band pass filters housed in the filter wheels during this study are as follows: The excitation filter for NADH is centered at 350 nm with 80 nm bandwidth (UV Pass Blacklite, HD Dichroic, Los Angeles, CA) and corresponding FAD filter is centered at 437 nm with 20 nm bandwidth (440QV21, Omega Optical, Brattleboro, VT). Moreover, the emission filter for NADH is centered at 460 nm (D460/50M, Chroma, Bellows Falls, VT) and for FAD is centered at 537 nm (QMAX EM 510-560, Omega Optical, Brattleboro, VT). Both emission filters have 50 nm bandwidth.

2.1.4 Camera

In this study a monochromatic EMCCD camera (QImaging®, Rolera EM-C^2, Canada) was used. This camera has low noise, high speed dynamic range, and high sensitivity in terms of signal detection. This camera possesses EM Gain that boosts the signal-to-noise ratio, and is suitable to acquire clear images under extremely low-light conditions [99]. The camera possesses a 1004 x 1002 light sensitive silicon chip near its optical interface that converts light intensity into an electric signal. (add sentence about converting signal to image.) The camera is mounted on a micro positioner which allows it to move backward, forward, and side-to-side easily.

2.1.5 Lens

The imaging lens is required component for image registration. A Canon standard zoom lens (EF 28-135mm, f/3.5-5.6 IS) with low distortions is placed in front of the CCD camera for the purpose of image formation. Because of the different mounting ports of the camera and lens a C-mount to F-mount connecter adaptor has been used to attach the lens and camera. The lens extends during zooming from its minimum length at 28mm to reach its maximum length at 135mm [100]. Due to a 1.6x cropping factor the zoom has a range of fields of view equivalent to ~45-216mm on full frame cameras.

2.2 Mechanical system and components

The unique features of cryoimaging setup including acquiring 3D images of tissue and producing high quantum yield, are possible mainly because of its mechanical characteristics. Sectioning tissues into slices provides layer-by-layer images of tissue required for 3D imaging. High quantum yield is provided by the low temperature experiment environment including tissue preparation and a temperature monitored freezer. The entire slicing system is housed inside the ultra-low temperature freezer.

2.2.1 Freezer

During an experiment, the organ is imaged in low temperature of -40^{o}C to preserve its metabolic state. In order to have a cryogenic temperature during the imaging, a large freezer with a viewing window on the side has been designed. The temperature inside the freezer is controlled by an accurate (±1C° sensitivity) interchangeable temperature sensor (Johnson Control, MR4PMUHV). In order to begin cooling the sample chamber, the freezer should be plugged in and the control switch should be turned on. It usually takes 2-3 hours to cool down to the imaging temperature (-40 c).

2.2.2 Microtome blade

Image quality, the smoothness of the imaged surface, and thickness of each slice, which determines the number of possible slices, are directly related to the blade employed for tissue sectioning. A microtome blade with capability of cutting extremely thin slices of tissue is used in the cryoimaging system. Briefly, two kinds of knives have been used in Cryo setup. One is a solid tungsten carbide, and the other one is a two- piece knife. The blade most often used in the experiments of this study is the two-piece knife (Delaware Diamond Knives, profile D,WC125cryo), which is a tungsten carbide tip cutting edge on a steel base. The parameters crucial to the performance and longevity of the blade are the clearance angle, specimen material, and the knife profile. The details are discussed in blade troubleshooting section.

The blade is mounted on the holder, as can be seen in Fig.2-6. The blade holder is then attached to the aluminum platform connected to the moving arm. A mechanical system is designed to provide blade movements and is powered by an AC motor (Blador, 1/3 HP AC motor VL 3501). The aluminum plate is connected to four pillow block bearings (Thomson, SPB-16-OPN) to smoothly move the blade side to side through the steel rails. Two micro switches (Honeywell, V3L-4-D8) are positioned on top of the pillow block bearings and control the limit of blade movement. Fig.2-6 shows the sensor and the position of the blade inside the cryoimager.

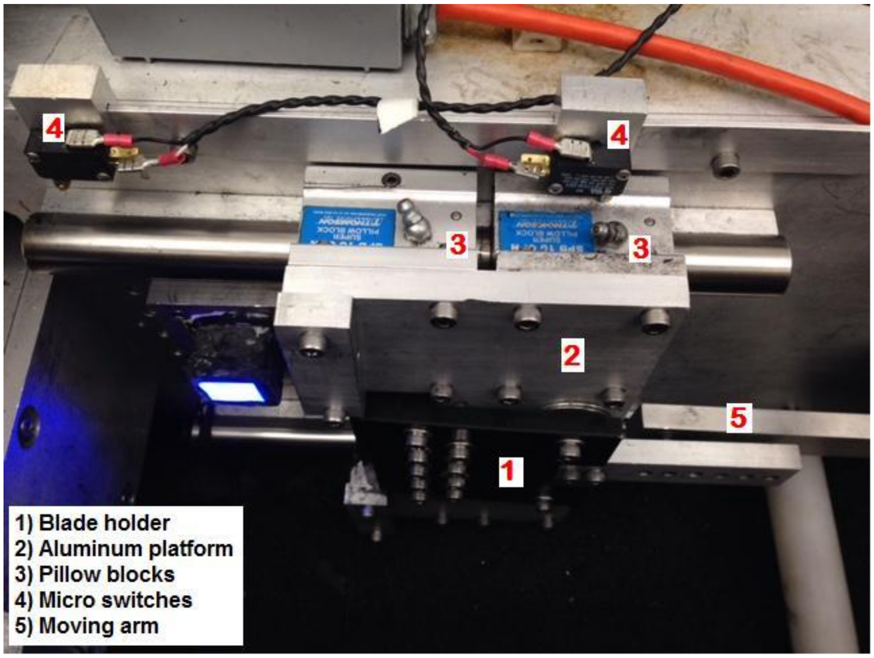

Figure 2-6: Inside the cryoimager

2.3 Software and automation

The cryoimager is an automated image acquisition system, and it is controlled by a written LabVIEW program. This user interface enables operators to easily control all of the hardware in action, record the images and display them while the slicing is in progress. By initializing the program, the software searches for all connected components, such as filter wheels, sample step motor, and camera. Without all proper connections, an error will occur in the software while initializing. The LabVIEW program has three primary panels: main, setup, and acquire. These panels are responsible for all aspects of the program. The main panel is the user interface which allows the user to monitor the cooling status of camera. The setup panel is the gateway panel, and allows for configuration and control of the majority of the cryoimaging subsystem, and the setting of the experiment parameters. The acquire panel is used to control the operation of the experiment. Most of the experiment parameters and adjustments can be set using the setup panel. The setup panel, as shown in Fig.2-7, includes four subpanels: Camera, File, Filter wheel, and Sample. Firstly, the user specifies the image destination for both NADH and FAD image channels. Then, the user specifies the positions of the desired excitation and emission filters using the Filter Wheel subpanel. By selecting the camera subpanel, a live image display window shows up, and camera configurations such as exposure time and gain can be modified through this panel while observing the results of changes on display window. The time duration that the camera shutter is open and light reaches the

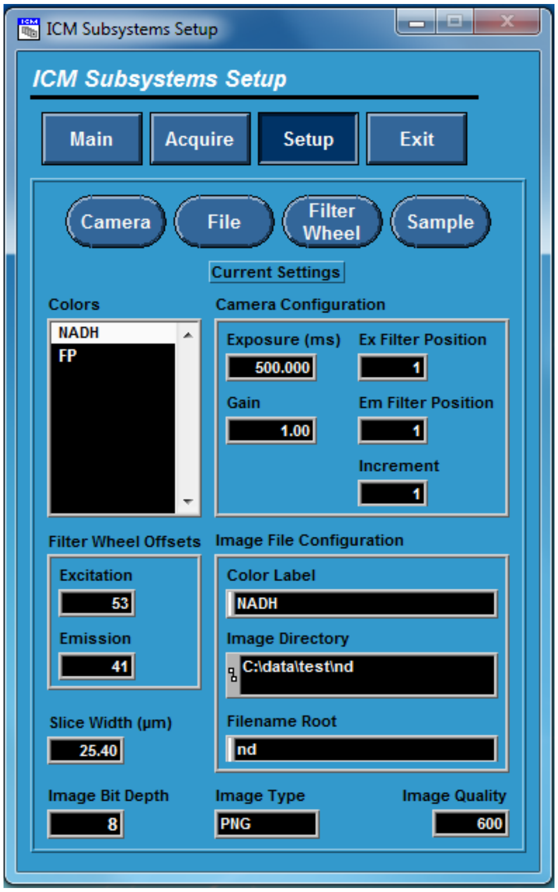

Colors: NADH, FP

Camera Configuration
Exposure (ms): 500.000
Ex Filter Position: 1
Gain: 1.00
Em Filter Position: 1
Increment: 1

Filter Wheel Offsets
Excitation: 53
Emission: 41

Image File Configuration
Color Label: NADH
Image Directory: C:\data\test\nd
Filename Root: nd

Slice Width (µm): 25.40
Image Bit Depth: 8
Image Type: PNG
Image Quality: 600

Figure 2-7: Setup panel of LabVIEW software

sensor, referred to as exposure time, is adjustable in range of 1msec to 59 minutes. The camera gain, which is the amount of analog electrical signal amplification, can be set from 0 to 4095 for the Rolera camera. Through the sample subpanel the position of the sample block can be adjusted where two micro-switches control the limit of sample movement range. The slice thickness is also set through the sample subpanel.

2.4 Linearity test

A linear response curve is a necessary condition for the reliable acquisition of signals. The linear response of the cryoimaging system has been evaluated using FAD and NADH concentrations in an aqueous solution. The range of NADH and FAD concentrations used in the linearity test span the normal NADH and FAD concentrations in typical tissues. The NADH solution concentrations range between 10 µM and 50 µM, moreover, the FAD solution concentrations are in the range of 50 nM to 250 nM that are

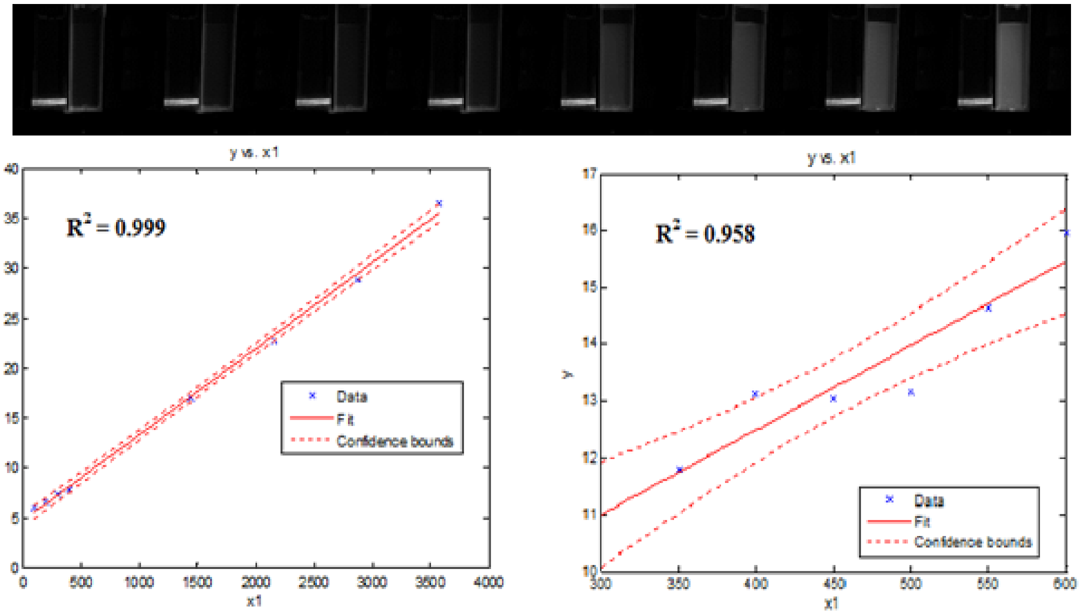

Figure 2-8: a) FAD solutions b) NADH solutions

comparable to tissue concentrations. Sensitivity curves of the cryoimager demonstrate a linear response to a change in the concentration of NADH (or FAD) in the presence of FAD (or NADH) over a wide range of NADH and FAD concentrations, as shown in Fig.2-8 Solid lines are linear regression fits. Linear regression resulted in R^2 of 0.958 and 0.999 for NADH and FAD, respectively.

2.5 Cryo-microscopy implementation

The newer version of our custom-made cryoimaging system is improved to increase the resolution of imaging in order to visualize the detailed information about structural changes in different organs. There are several diseases, such as cardiopulmonary injuries and diabetes that cause structural changes, especially in the vasculature. The cryoimager has the microscopy capability to monitor the structural changes as an effect of the disease and correlate the results with metabolic changes in the tissues.

The cryo-microscopy setup is different compared to the cryo-macroscopy setup and the schematic of optical path of cryo-microscopy is presented in Figure 2-9. As you can see from this figure, the excitation path of the microscopy setup is the same e as macroscopy. In favor of decreasing the working distance, a large filter wheel has been replaced with a small one. The filter wheel is mounted between the lens and camera, so that emitted light coming from the tissue surface first encounters the lens, then passes through the emission filter wheel, and ultimately reaches the camera. The cryo-microscopy setup is also equipped with raster scanning to be able to image large samples, such as rat kidneys. The additional component using in microscopy setup is as follows:

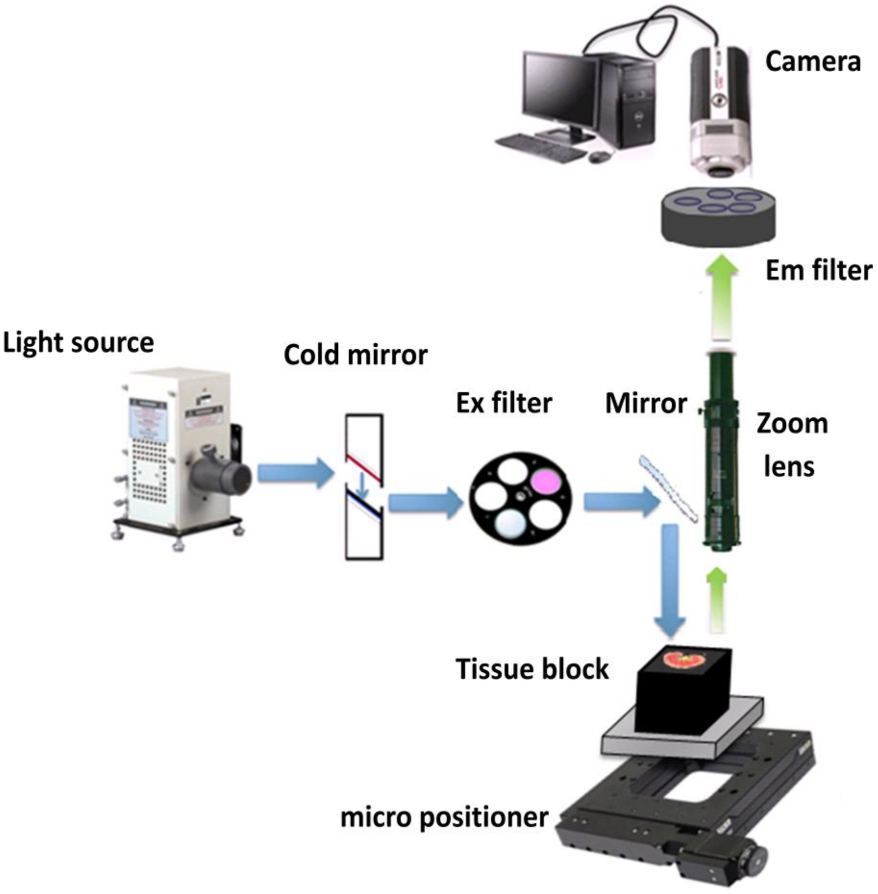

Figure 2-9: Excitation and emission path in cryo-microscopy design.

2.5.1 Zoom lens

The utilized lens in the system is an Optem Zoom lens (125C 12.5:1 Micro-Inspection, Qioptiq), which provides magnified images by holding high resolution. This lens is able to magnify the image up to 6.5X without any auxiliary lens, and the working distance with this parameter would be 89 mm. Since the minimum working distance of the cryo setup was 98 mm, we used a 0.75 auxiliary lens in order to increase the lens' working distance up to 114 mm [101]. Resolution is defined in number of line pairs per millimeter (LP/mm). Each pair consists of a black line and a white line. Higher LP/mm means higher image resolution [102, 103]. By adding the 0.75 auxiliary lens the magnification is ranging from 0.39X to 4.9X which results the resolution of 42 LP/mm and 217 LP/mm, respectively. The other advantage of using the Optem zoom lens is having the small focal shift.

2.5.2 Linear micro stage

The optical lenses have the chromatic aberration, which is focusing different wavelength in different focal points. As I mentioned before we are imaging two fluorophores, NADH and FAD, and the emission wavelength of these fluorophores are different. Therefore, the NADH image and FAD images have shifted focal length due to the chromatic aberration. It means without refocusing, image in one of the channels always becomes blurry in high resolution images. The camera is installed in a linear translation micro-stage (NRT 150, Thorlabs with 150mm moving distance) to be able to move the position of the camera in order to eliminate the chromatic aberration of the imaging lens.

2.5.3 Raster scanning

Magnification of the images resulted in losing the field of view, which means the whole tissue cannot be imaged once at time for larger samples. Raster scanning is a solution to this problem. Raster scanning is implemented by subdividing the image into several fields of view, and taking images of each single field of view. Then these single images will be stitched together to construct the whole image. For raster scanning, movements in two directions (X and Y) are required. To implement raster scanning we have used a two-axis motorized micro stage (Standa 8MTF - Motorized XY Scanning Stage). The stage is vertically installed in the cryo freezer chamber and the tissue block is mounted onto it. A sample image from raster scanned kidney, and reconstructed image is presented in Figure 2-10. More details of cryo-microscopy setup have been reported previously [104].

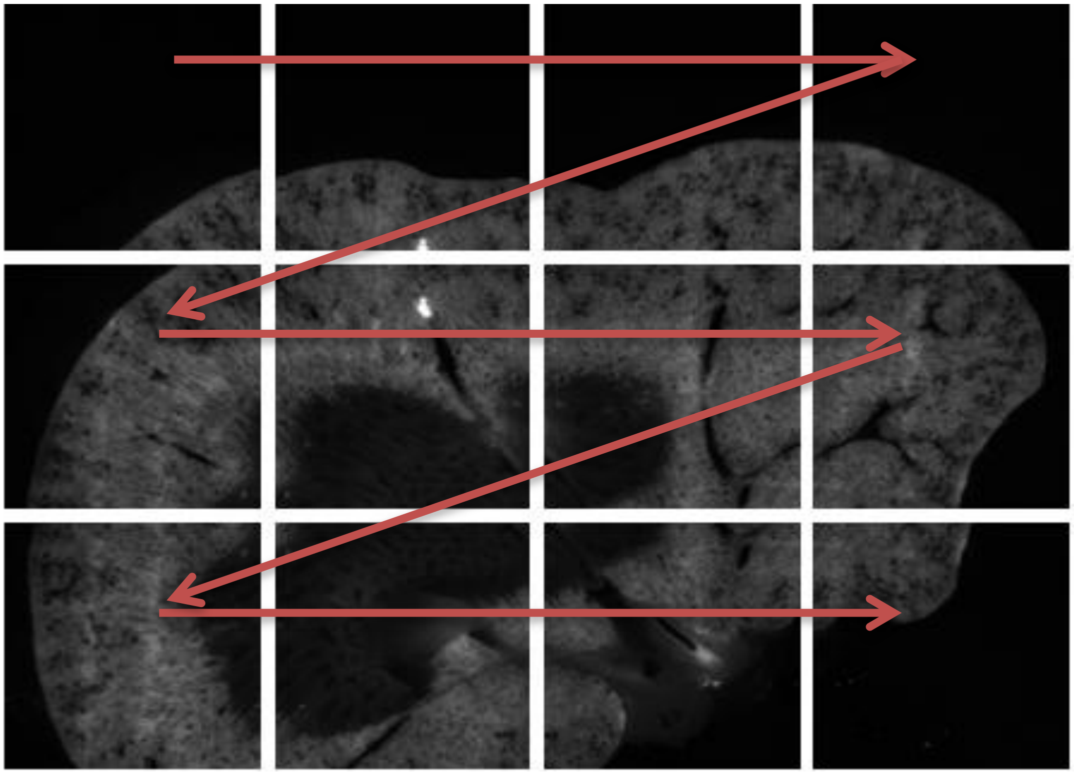

Figure 2-10: Multiple fields of view of one slice of a rat kidney sample with cryo-microscopy setup.

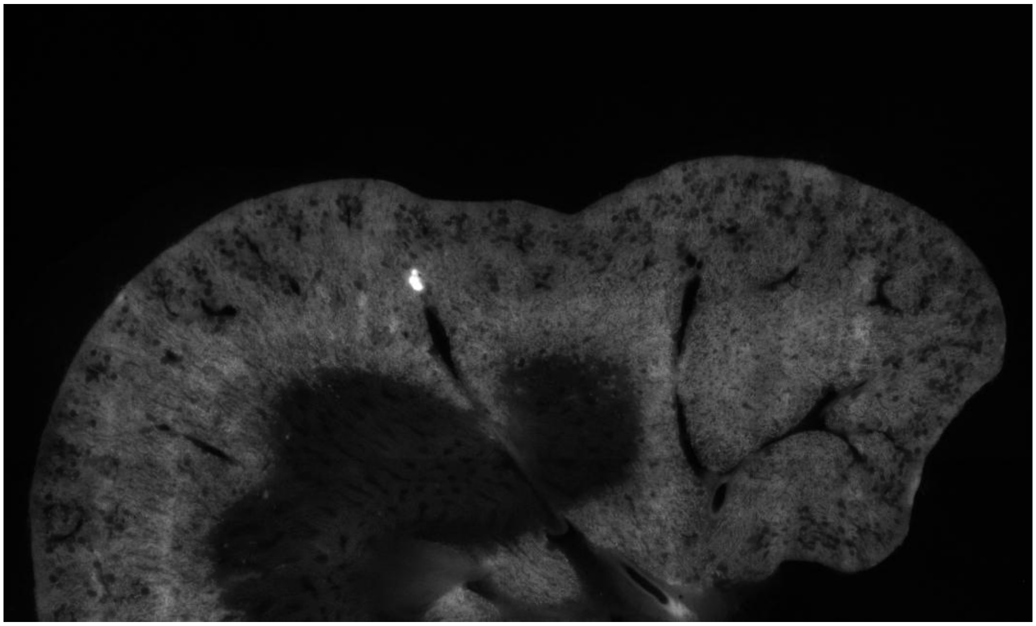

Figure 2-11:Stitched fields of view of one slice of a rat kidney sample.

2.6 Cryo System optimization and troubleshooting

The cryoimaging system includes optical, electrical, and mechanical components. Like any other systems wear in the hardware units will result in problems arising over time. Failure in any of these units would affect the final result. More importantly, each of these elements should be accurately adjusted to achieve the optimum operation of the cryoimaging system. Herein the most likely challenges, possible causes, and the method to mitigate the issues and optimize the device operation are discussed.

2.6.1 Sectioning problem

The quality of acquired images is directly influenced by tissue sectioning. Smoothness of tissue surface ensures the fine image acquisition. A slight angle in tissue cut results in a change of working distance for part of the sample, resulting in some areas being out of focus, causing obscure image. Sectioning results with a tungsten carbide knife are affected by section thickness, sectioning speed, block hardness and clearance angle setting. It is very important to know how any changes in these operating parameters will affect sectioning quality. Sectioning problems usually come in three forms: chatter, compression, and knife marks.

Chatter is the result of vibration during cutting and appears as regularly spaced thick and thin lines on the section perpendicular to the direction of the cut (Fig.2-12 (a)). Low clearance angle, too fast of an approach and too hard specimen are several possible causes of chatter.

Compression is the crushing of a section as it is cut resulting in a section that is shorter than the original block face and thicker than the microtome setting (Fig.2-12 (b)). Usually too high of a clearance angle, too soft of a specimen, and a dull knife can cause compression. Finally, knife marks are lines that appear on the section parallel to the direction of cut (Fig. 2-12 (c)). A dirty or damaged knife edge causes knife marks.

Prior to performing any maintenance, the type of artifacts should be identified followed by constructive steps taken to overcome the sectioning problem. In general, knives should be sharpened after 15,000 slices or when necessary. This would solve the knife mark risk and any other problem caused by a dull blade. In following, the other two most effective parameters that should be considered when facing a slicing problem have been discussed.

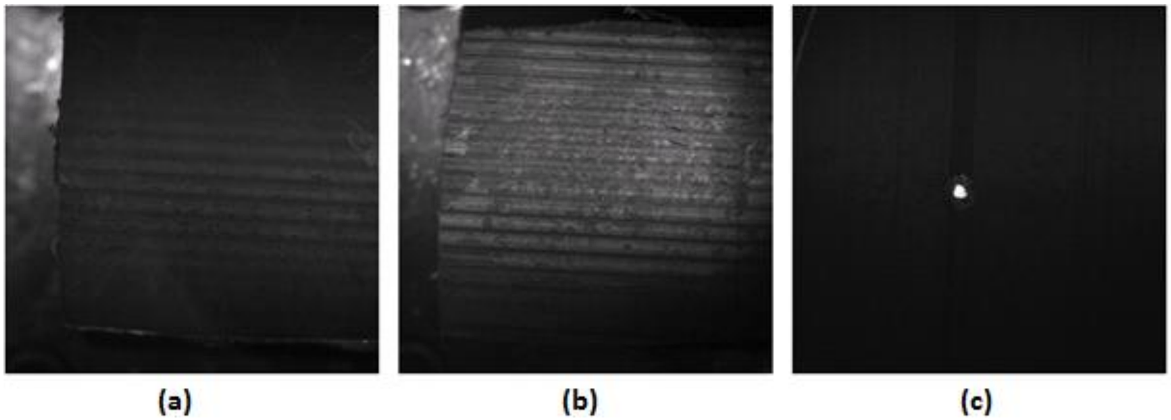

Figure 2-12: sectioning patterns: (a) chatter (b) compression (c) knife mark

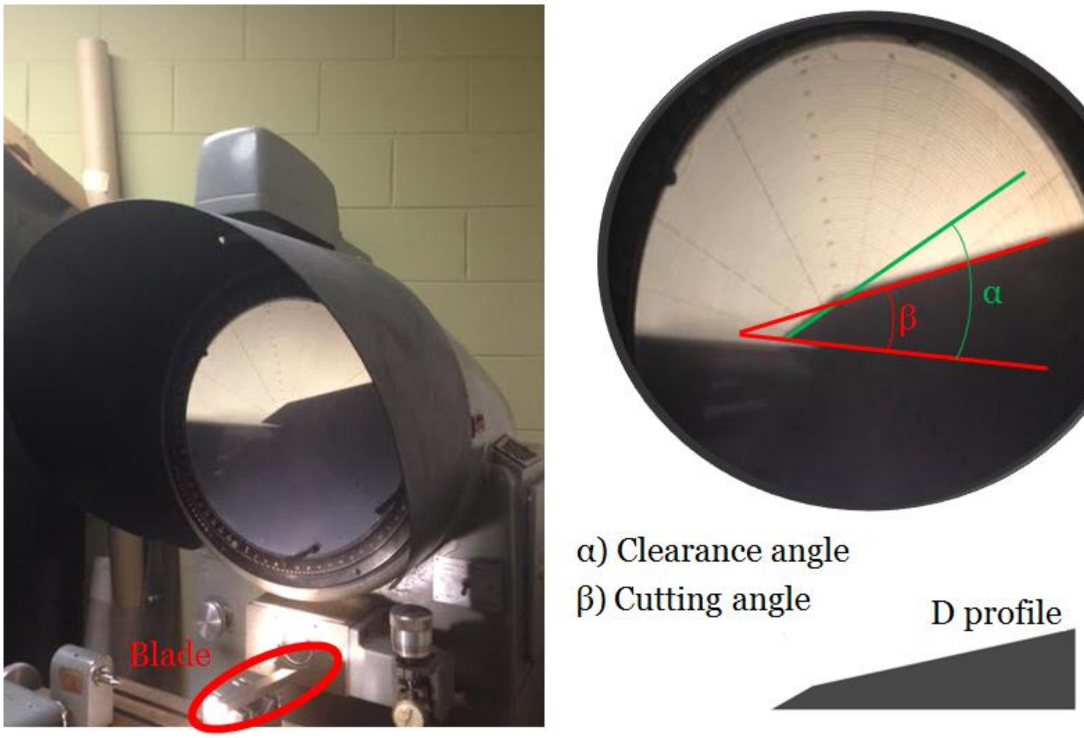

Figure 2-13: Shadowgraph and blade angles

Optimal clearance and cutting angle

The microtome blades are characterized by their profile and two main angles named: clearance and cutting angle. The clearance angle prevents contact between the knife facet and the face of the block. The clearance and cutting angles of the cryoimaging blade are approximately 35^o and 30^o, respectively. A shadowgraph has been utilized to measure the blade angles (see Fig.2-13); both angles are represented in the highlighted shadow of the actual blade in the cryoimaging system.

The cutting angle is an inherent characteristic of the blade. The clearance angle is adjustable while mounting the blade on the holder. There is a clearance angle in which blade performance is optimal. In order to set the blade clearance angle optimally in the cryoimaging system, the following steps should be accomplished: first, the blade should be removed from the holder and from the aluminum platform. This is feasible by unscrewing the row of two and four bolts (Fig.2-14). Second, the row of five screws should be loosened as much as needed; these screws hold the blade in place, and then the blade could be easily removed by sliding it out. The third step is cleaning the blade and holder with alcohol. The fourth step is to put the blade back and tighten the row of five screws eventually. This should be done by carefully, tightening all the screws progressively, rather than tightening one by one. If one is tightened too much this will affect the final angle adjustment. The last step would be to reattach the blade to the aluminum platform. For appropriate clearance angle adjustment, two washers with specific thickness are placed underneath each screw in the row of two screws.

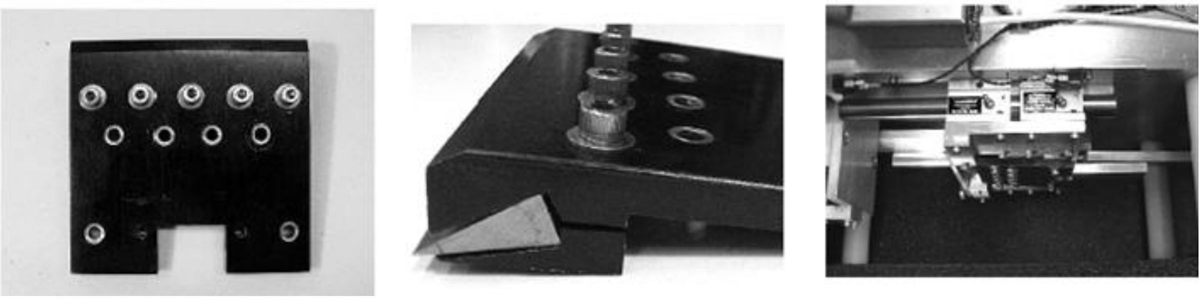

Figure 2-14: Blade holder

Blade arm vibrations

The blade arm vibration is another possible issue that causes noise and disturbs the blade function. Horizontal movement of the blade arm originates from a rotating motor. The arm linkages convert the rotary motion to the linear motion, which advances the blade toward the sample and backward. Several cylindrical bearings have been used at the connections of these arms. As mentioned before, the pillow blocks are also used to ease movement of the blade toward the sample along the steel rails.

Several things could cause these vibrations, such as: damaged bearings, insufficient lubrication, tilted rails and arms, or warped platform. In order to prevent the rotary mechanic part from damage, regular service is needed.

2.7 Tissue preparation for cryoimaging

Experimental procedures were approved by UWM and Medical College of Wisconsin Institutional Animal Care and Use Committee (IACUC). Male rats were obtained as weanlings from colonies maintained at the Medical College of Wisconsin.

Kidney tissues from rats were used in the frozen tissue studies. Each set of tissues has been prepared distinctly; a brief description of our tissue preparation protocols are as follows. There are several steps to prepare the sample for cryoimaging, including tissue preparation, sample freezing, mounting medium preparation, and sample embedding. These steps are explained in more detail in the following sections.

2.7.1 Freezing Protocol and Embedding

Freezing: In order to preserve the metabolic state of the kidney tissue, it has been rapidly frozen in cooled isopentane (2-methyl butane, Fisher Scientific, IL) cooled by liquid nitrogen (LN_2, -196^{o}C). When it is close to reaching the correct temperature the isopentane starts to become opaque as it nears freezing. The hemisected kidney is dropped into a container of isopentane for 5-10 seconds, and then tissue is removed to

LN_2 container for 2 minutes. Finally, the hemisected kidney was wrapped in in tin foil for permanent storage at ultralow freezer (-80^{o}C) until imaging was performed. This method has the advantage of very rapid freezing without causing cracking due to sudden temperature change. For fluorescence imaging, the tissue was embedded in a customized black mounting medium, which is not fluorescent in the excitation wavelengths, and placed on a chilled aluminum plate to keep the tissue in place for freezing and slicing.

Mounting medium: The mounting medium was prepared in the Biophotonics lab (UWM), using polyvinyl alcohol (PVA, Grade 71-30, PVOH7130, Chemical Store Inc.,Clifton, NJ), distilled water and Indian ink. To make one liter of the black mounting medium, 80 g of PVA is mixed into 920 g of cold distilled water and stirred until the PVA completely dissolves. The liquid is heated at 300 ^{o}F for 1.5 hours. The solution should be stirred while it is boiling until the liquid becomes transparent and dense. Prior to adding Indian ink, the temperature of the solution should be turned down (250 ^{o}F) to stop boiling. Enough amount of ink should be added and mixed thoroughly to make the entire solution black. Heating at (250 ^{o}F) will continue for 30 minutes, and then the

Figure 2-15: Black mounting medium preparation steps

solution is allowed to cool down to room temperature. The mixture is stored in the regular refrigerator until needed. Several steps are showing in Fig.2-15. One day before use, the mixture is placed on the rotary motor rock tumbler to mix and warm up to room temperature.

Embedding: Prior to embedding the tissue, an aluminum stand has been frozen (Fig.2-16 (a)) and a mold with four Teflon pieces is prepared (Fig.2-16 (b)). The tissue is also trimmed to remove fats. The first step in embedding a tissue sample is to sit on the mold on a chilled stand, pour the black mounting medium inside to make 0.5 cm thick base. The embedding process follows with freezing the base medium, then embedding the tissue and fixing its position by adding more black medium around the tissue. After embedding, the tissue is stored in an ultralow freezer (-80^{o}C) for at least 4 hours. (Fig.2-16 (c)) shows a sample block ready for cryoimaging. Before starting the experiment, the sample stand is installed on the sample carriage in the cryoimager using four nuts such that the surface of the black medium is parallel to the cryoimager microtome

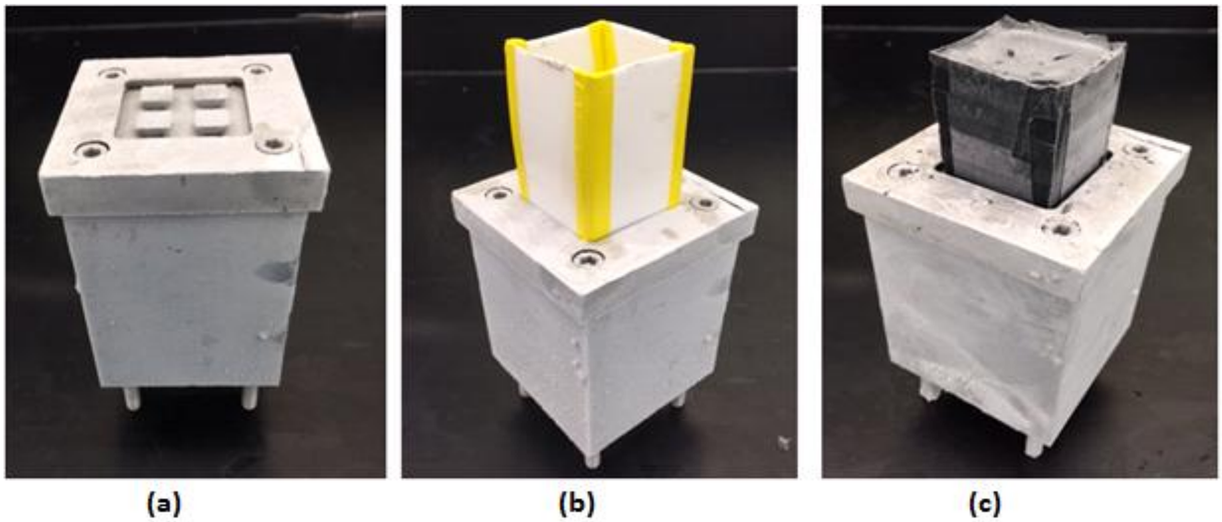

Figure 2-16: Sample embedding steps

Chapter 3: Image processing

Overview

Raw data collected from cryoimaging has been enhanced and analyzed using image processing tools. The acquired raw images of NADH and FAD fluorophores from each group of kidneys were analyzed using MATLAB software. Before quantifying the redox, raw images were preprocessed to compensate day-to-day variations, such as light intensity, illumination pattern, and mirror angle. Then, an automated algorithm was implemented to remove the undesired background of the images. After preprocessing and calibration, three dimension representations of the kidneys were rendered using z-stacks of all the image slices (about 400 images for each kidney), for both NADH and FAD channels. In the following section, details of each step are provided.

3.1 Preprocessing of raw images

As discussed in the previous chapter, gathering experimental data requires running the experiment for a few days. During this time, there are a few possible problems that could affect the quality of final results, such as change in light intensity, mirror angle, and illumination pattern. In order to exclude any possible variation and make the necessary corrections, preprocessing was carried out both in MATLAB and ImageJ software. Each step to correct these problems has been explained in detail in this section.

In the experiments conducted for this thesis, the thickness of each slice was adjusted to 30 µm. Based on this thickness, each kidney sample resulted in 300 to 400 images in each of the NADH and FAD channels.

3.1.1 Lens focusing and image scale measurement

At the beginning of each experiment, a piece of grid paper was placed in front of the camera and right on top of the embedded tissue. This grid was used to set the focus of the lens, as shown in Fig.3-1 (a). This image is referred to as the grid-image. The grid-image was also used to determine the resolution of each experiment. In order to examine the resolution, the number of pixels within a known distance on both the x- and y-axis was counted to get the number of microns per pixel in the horizontal and vertical directions.

3.1.2 Dark current noise correction

For each different camera setting used in the experiment, the dark-current image was captured before image acquisition. A representative dark current image of the experiment has been shown in Fig.3-1 (b). In order to collect the dark-current image, the lens of the camera was covered and the lamp was shuttered. Dark current noise correction was done by subtracting the appropriate dark-current image from the experimental images.

3.1.3 Non-uniform illumination correction

The light source used to illuminate the sample is not perfectly uniform on the surface plane of the sample. Also, the lighting pattern slightly changes for each experiment set. Before slicing the tissue, a uniformly yellow-green fluorescent acrylic plate that was completely flat was placed at the position of the tissue. In the same field of view in which the grid-image was acquired, an image of the flat plate was captured in both NADH and FAD channels. These acquired images are called flat-field images. The flat-field images should not be saturated in order to be used for correcting distortions caused by day-to-day light intensity variations, as well as possible non-uniform illumination on the sample (Fig.3-1 (c,d)). The acquired dark-current image was subtracted from the flat-field image, and then to correct experimental images for non-uniform illumination, all the data images were divided by the resulting difference image.

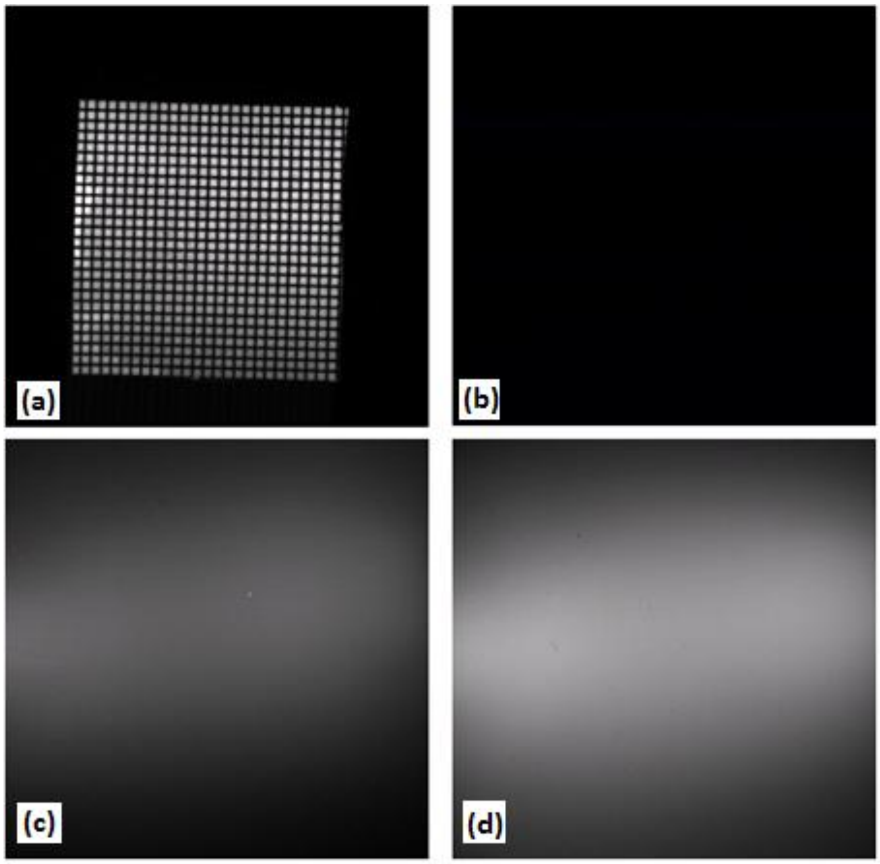

Figure 3-1: (a) Grid (b) Dark current; Fat field in (c) NADH Ch. (d) FAD Ch.

3.1.4 Shadow correction

Sometimes a shadow in the images was observed. Because the cryoimaging setup is sensitive to background noise and vibration, this could be caused by a small movement in the mirrors, any other movements, reflection from metallic materials, and the displacement of the black curtain cover. To correct for the shadow, a shadow pattern is obtained by subtracting two consecutive images, one just before the appearance of the shadow and one afterward. The shadow pattern (Fig.3-2 (c)) is removed by subtraction of this difference from the all of the affected images. The (Fig.3-2 (b)) and (Fig.3-2 (d))

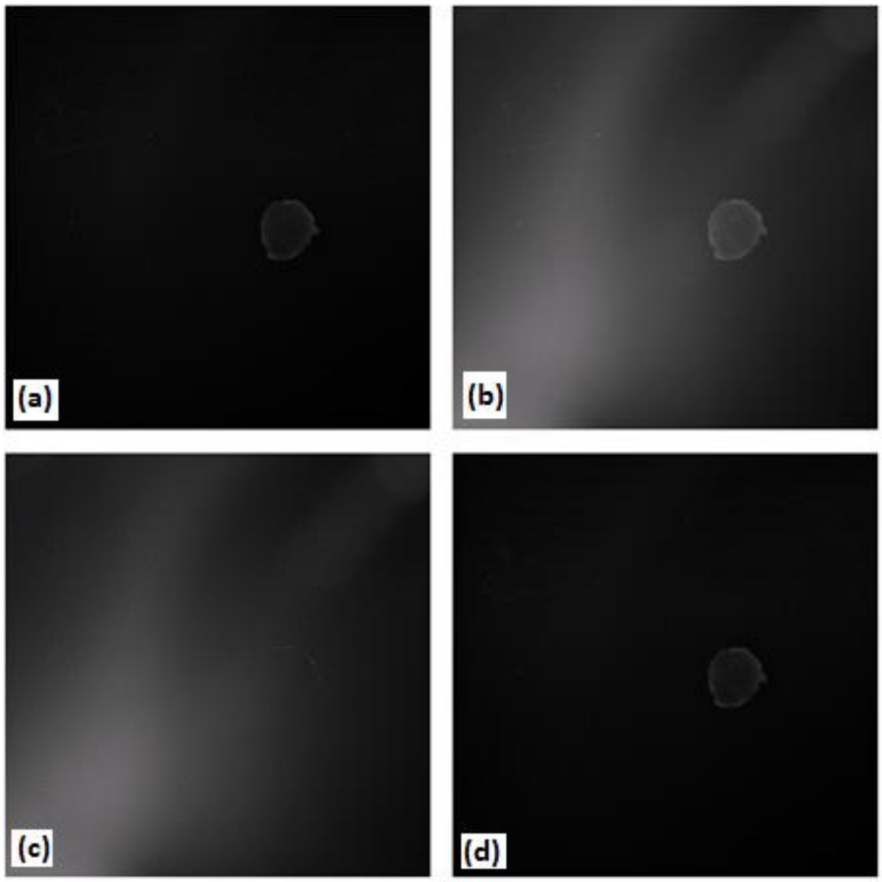

Figure 3-2: Shadow correction steps

shows an image affected by shadow and corrected image respectively, and for comparison, (Fig.3-2 (a)) shows an unaffected image.

3.1.5 Removing and replacing defective image

In the process of slicing and imaging, sometimes a previously sliced tissue layer could cover part of the sample surface and blocks the camera’s view, leading to a partial dark area in the next image. Since this image doesn't contain any information about the sample, it is useless and should be discarded. Figure 3-3 shows two samples of defective slices in the NADH channel that are removed in this step. Both image stacks of NADH and FAD were checked for removal of these undesired slices. A single unwanted image is going to be removed in the stack. If there were more than a couple of defective images in series, instead of copying previous and following images, a creeping median filter of 3 images was used.

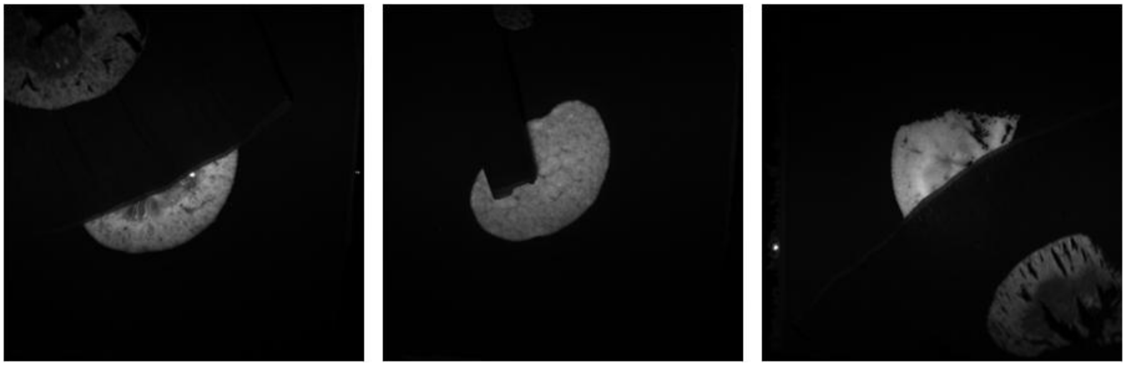

Figure 3-3: Defective Images

3.1.6 Intensity and exposure changes corrections

Usually at the beginning of the experiment, exposure is set to a desired value. However, because of the uniqueness of the illumination for each sample, especially for a new sample, sometimes it becomes necessary to modify the exposure in the middle of experiment. This is to prevent saturation or to improve the contrast. There are also other factors that might cause a sudden increase or decrease in intensity during the experiment. Figure 3-4 shows two consecutive slices in an imaging experiment in which the exposure time was increased by the operator to increase tissue intensity, in order to improve the contrast of images. In the image processing, a linear scaling factor is used to compensate for the intensity change.

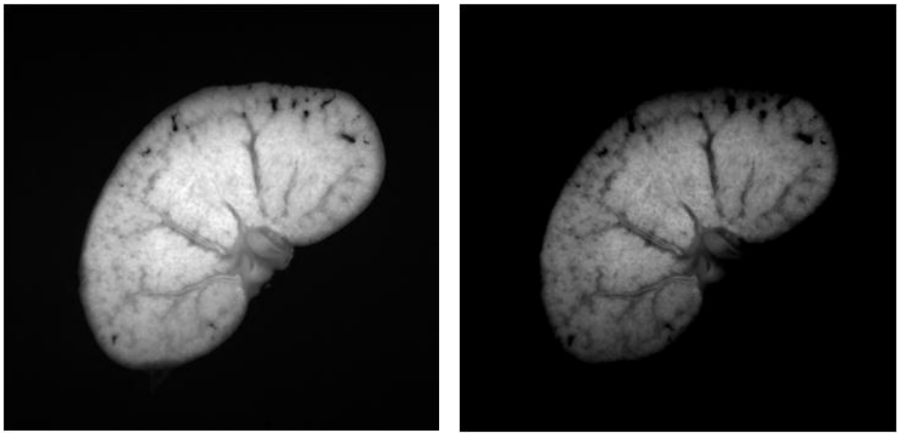

Figure 3-4: Different exposures in NADH Ch.

3.1.7 3D representation of sample and present from specific cross section

As mentioned earlier, each kidney experiment results in 300-400 images and it is time consuming to check them one by one to remove the defective images. An easy method is to reconstruct a 3D structure from the preprocessed stack of images and check the resulting 3D image from different views. If, for any reason, some part of the sample was missed or an unwanted slice was included, it is simply visible in the 3-D structure. A proper 3-D reconstructed image of a kidney can be seen in Figure 3-5.

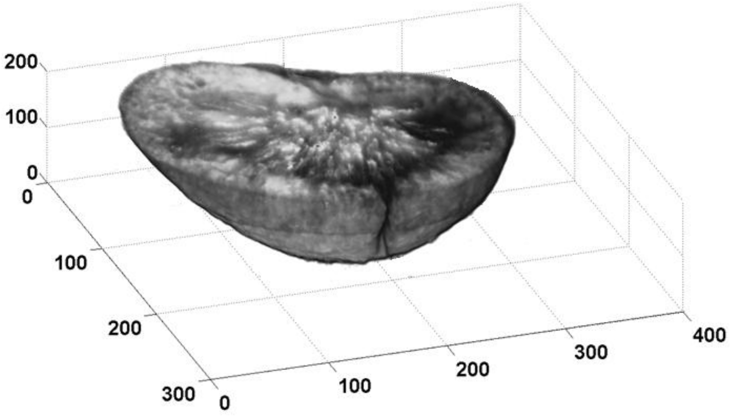

Figure 3-5: 3D rendered of a kidney

It is also possible to filter the 3D volume of the tissue in such a way that a specific cross section or a targeted region of tissue is highlighted. For example, a 3D-rendered representation of hemisected kidneys could be presented in a view that shows the structure inside the kidney and allows the examination of the differences between the medulla regions. The cross-sectioned 3D rendering was performed by defining a tilted plane in the 3D volume (using the voxels' inherent coordinate geometry), and filtering the image on either desired side of the tilted plane (see Figure 3-6).

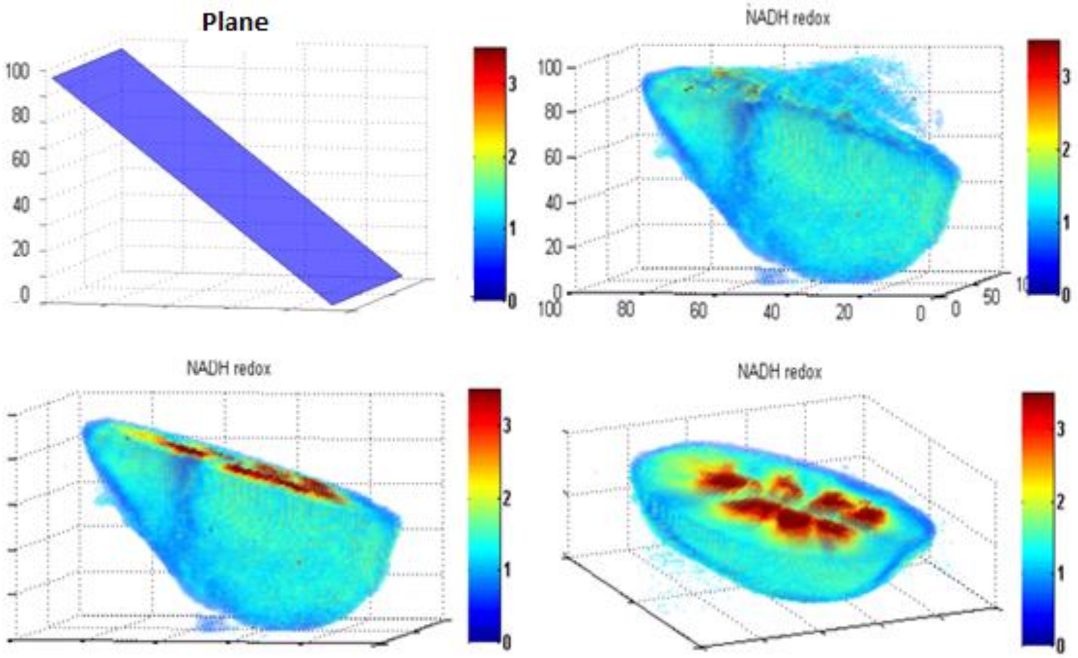

Figure 3-6: Specific cross sections

3.2 Boundary detection and background removal

Analysis of multiple cross-sectional images of a kidney has many problems. Micro slicing of each kidney produces around 400 slices. Sometimes, due to low contrast of the image and problems with the mounting medium, it is difficult to remove the background by thresholding. In the other words, some part of the sample in a 2D cross sectional image has an equal or lower intensity compared to the background, so removing the background simply by thresholding will cause a deletion of some of the tissue pixels. Usually, the first step to analyze all of the slices of a sample is background removal, which is manually done by employing ImageJ. Manual background removal is time consuming, user-dependent, and results in variation between different slices. Since the size of the object changes in each slice, manual edge detection is a laborious task.

Creation of the 3D-rendered image of a tissue also suffers from the aforementioned problems, especially in high resolution imaging. Removing the background is essential, otherwise the output would be a black box that shows the medium where the tissue is embedded. Manual selection of the borders results in an unsmooth surface in the 3D image. The thresholding method also increases the noise around the tissue and removes some tissue features due to the low contrast between some parts of tissue and background. To overcome this problem, an automated algorithm has been designed to determine the border of the cross-sectional images of the kidney in different z-depths, removing the background and enhancing the contrast of the result. In the following section, a brief introduction of the image processing concepts has been described, and the proposed algorithm has been explained in detail.

3.2.1 Morphological image processing

The term morphology refers to the properties of the geometric structure of any object. Operations of mathematical morphology were originally defined as operations on set theory, but it later became clear that they are also useful for image processing tasks by performing operations on a set of points in a two-dimensional space, like an image. Sets in mathematical morphology represent objects in the binary image. For instance, the set of all background pixels of a binary image (zero values) is one set which could be defined in an image. Mathematical morphology operators are the main tool used to extract the structures present in the image. These structures are useful for quantitative analysis of the image. For example, some structures that can be extracted are contours, skeletons and convex hulls. The most elementary operators of mathematical morphology are erosions and dilations. More complicated morphological operators such as thinning and thickening can be designed by means of combining erosion and dilation operations. Also, morphological methods are used in the preliminary and final image processing [105].

3.2.2 General algorithm implementation

An edge detection package has been developed to find the boundary of the tissue and clear the background of the images. This algorithm has been written in MATLAB (The MathWorks, Inc). Figure 3-7 shows the flow diagram of the basic coding process for a stack of images. The procedure was initiated by loading the slice that contains the largest portion of tissue in the stack of the images. A region of interest (ROI) was selected around the tissue to get rid of extra calculation and minimize the memory usage.

In the next step, the ROI position was applied for each slice of the tissue and the image was cropped. Separate folders were produced and located in the same directory to store the output images and preserve the raw data. After cropping the image, the feature is detected using the edge detection algorithm, and the background has been removed. The details of the edge detection algorithm are described in the next section. Following the removal of the background, contrast enhancement has been done using a histogram equalization method to improve the appearance of the structural features in the 3D rendered image. Both the background image and contrast enhanced image are stored in their defined directories.

The aforementioned steps have been carried out on every single slice of the stack in both the NADH and FAD images.

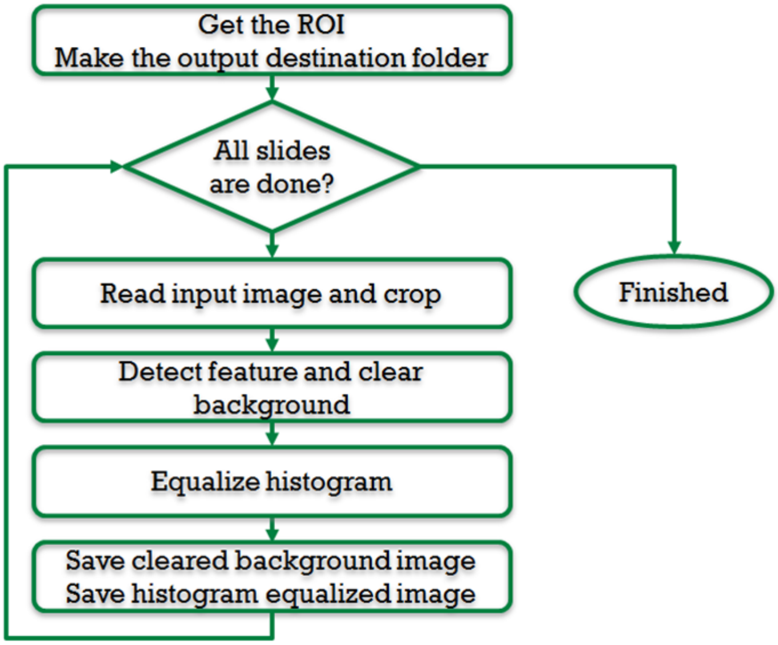

Figure 3-7: General boundary detection algorithm

3.2.3 Proposed boundary detection algorithm

Figure 3-8 shows the flow diagram of overall methodology to find the boundary and extract the feature from the background. The details of the edge detection algorithm are as follows.

First, the cropped image is smoothed using a 5×5 Gaussian filter, as a low pass filter, to reduce some machine-induced artifacts, and image noise (Fig.3-9 (b)). Mathematically, applying a Gaussian filter to an image is the same as convolving the image with a Gaussian function. Image pre-smoothing is applied prior to the edge detection in order to obtain better results. Pre-smoothing also helps to improve global thresholding.

Secondly, the gray scale smoothed image is converted to a binary image by

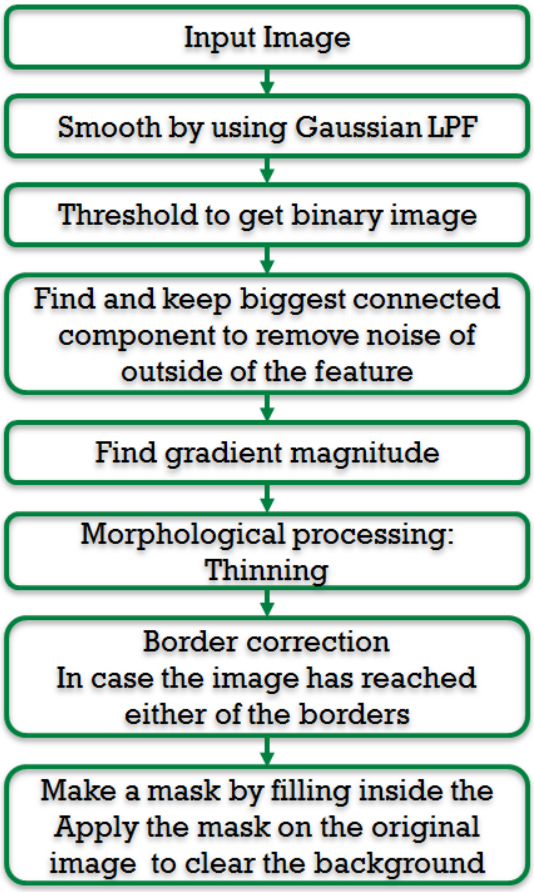

Figure 3-8: Proposed boundary detection algorithm

selecting an appropriate threshold, as shown in Fig.3-9 (c), where all pixel values in the input image with luminance greater than threshold level are replaced with 1 (white) and all other pixel values with 0 (black).

Thirdly, after generating a binary image, the connected components were found in the binary image, and because the tissue is the dominant part of the image the biggest connected component has been considered to be the tissue (Fig.3-9 (d)). This is an efficient way to remove extra noise and dots which are surrounding the feature.

The fourth step is the sharpening of the cleaned binary image by means of a Laplacian filtering to enhance discontinuous regions such as edges (Fig.3-9 (e)). High-pass filtering can “enhance” the high-frequency (lines and edges) while “suppress” the low-frequency (smudge regions). Following the sharpening of the image, the gradient magnitude of the image was calculated. The gradient was used to enhance sudden changes and eliminate slowly varying background features. In this process, pixels with large gradient values are more likely to be the edge pixels. The high gradient pixels that are in the direction of the gradient are considered edge pixels, and edges are traced in the direction perpendicular to the gradient direction.

The next step is applying a thinning operator to the binary image to tidy up the output of previous step by reducing all lines to single pixel thickness.. In other words, thinning is particularly useful for skeletonization (Fig.3-9 (f)). Before moving to the next step, the border corrections have been done. This is particularly for the cases that tissue exceeds camera’s field of view, and continues over the image border. Border correction includes a modification in pixel values adjacent to the image border to consider them as edge pixels and have a connected boundary.

Finally, the hole regions encircled by the edge were filled and a mask was produced to extract the feature from the background (Fig.3-9 (g)). A hole is defined as a background region surrounded by a connected border of foreground pixels. This mask could be applied to both NADH and FAD channel slices, so a composite binary mask image was created from each slice. The algorithm terminates by multiplication of the mask and original image to remove the background (Fig.3-9 (h)).

As a summary, the morphological edge detection implemented is an effective method for finding the border of the images and clearing the background. By removing the background of the slices, the accuracy of data analysis has been improved. This program automatically performs elimination of the background, which is essential to have a smooth, artifact-free 3D rendered image. By using this program, a considerable amount of time was saved in the image processing part of my research.

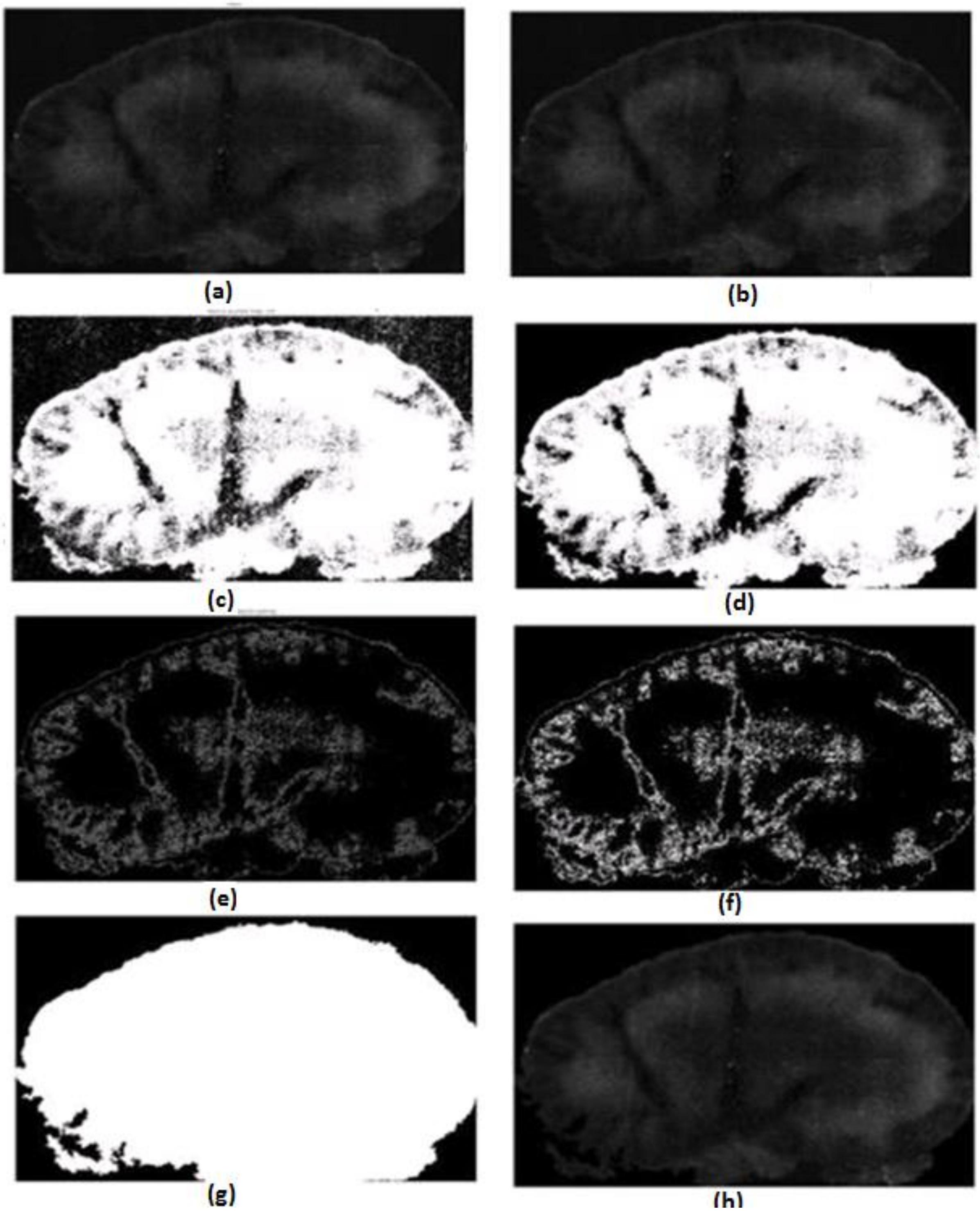

Figure 3-9: Background removal algorithm steps

3.3 Redox calculations and data representation

The pre-processed FAD and NADH fluorophore images from each group of kidneys were analyzed using MATLAB. Three dimension representations of the kidneys were rendered using z-stacks of all of the image slices, for both NADH and FAD signals. The intensity at each voxel in the NADH and FAD images is used as an indicator of the concentration of the fluorophore at that voxel. The NADH Redox ratio of each slice of kidney was calculated pixel by pixel, using MATLAB, according to equation (1).

$$\text{NADH Redox Ratio} = \text{NADH RR} = \text{NADH} / \text{FAD} \qquad (1)$$

Then, the corresponding histograms, which are distributions of intensities in 3D volume, were plotted. The histogram is a scaled probability density function of the mitochondrial redox ratio intensities in a kidney used for quantitative analogy between the groups. The arithmetic mean values of the histograms were calculated according to Eq. (2)

$$Mean = \frac{1}{N_x \times N_y \times N_k} \sum_{i=1}^{N_x} \sum_{j=1}^{N_y} \sum_{k=1}^{N_k} kidney\_Volume(i, j, k) \qquad (2),$$

where $N_{x,}$ N_y and N_z are the number of pixels in the x, y and z directions. In my studies, the pixel size in the x and y directions were 10µm, but in the z direction was 30µm. There are three methods to present the data, which are described in following section. The final presentation method was selected based on the purpose and desired part of the tissue.

3.3.1 Different methods to present the data

In this part the three methods are reported for representation of the results. Each method has its own advantages and disadvantages which are mentioned in following:

The largest slice representation and focus on specific region

In this method, the slice with the most tissue from the image stacks is chosen to present the Data. Especially when we need to examine the differences in a region of interest such as medulla this method is useful. Figure 3-10 shows NADH, FAD, and NADH redox images from the biggest slice of a salt-sensitive kidney.

The disadvantage of reporting the data using a single slice is that it introduces a sampling error in which the result is only dependent on one slice and may not precisely represent the overall tissue's redox state. However, this method is useful to focus on a specific region of the tissue, which is of more interest. For example, the renal medulla of the kidneys can be segmented and their corresponding histograms are compared to examine the regional injury.

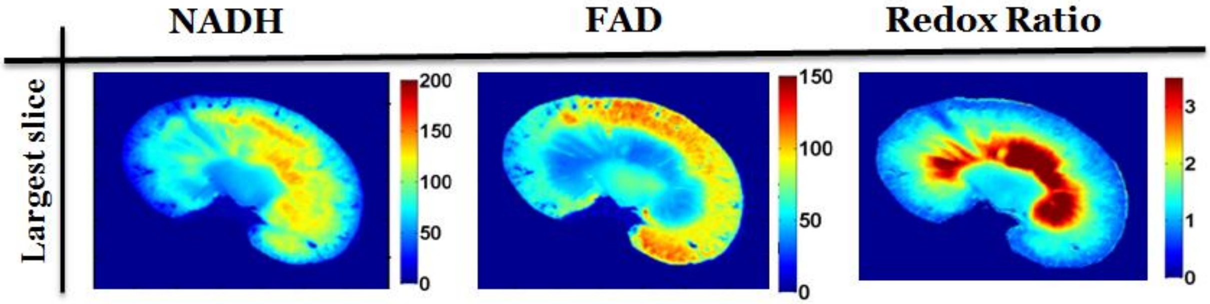

Figure 3-10: The largest slice representative panel

Maximum intensity projection representation

In this method, the maximum intensities along the z axis of the NADH, FAD, and redox ratio z-stack were obtained and results a 2-D representation to compare the data of different groups. Figure 3-11 shows the maximum intensity projection of NADH, FAD, and NADH redox in a salt-sensitive kidney.

The maximum intensity projection method is advantageous in that it may highlight the details that are not observed in the other methods. For instance, the vascular dysfunction in kidney caused by hypertension can be shown using this method.

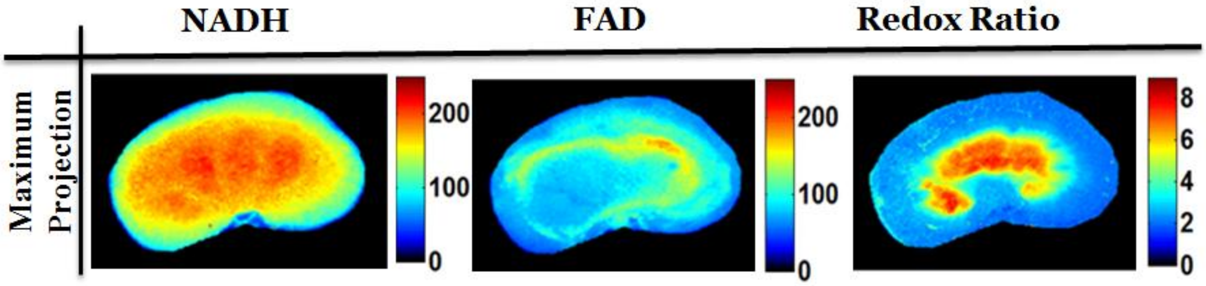

Figure 3-11: Maximum projection representative panel

3D rendered representation

In this method, the 3-D composite images created from all of the slices are used for representation and comparison of the data and calculation of the histograms. Figure 3-12 displays the 3-D rendered NADH and FAD images and the NADH redox of a salt-sensitive kidney.

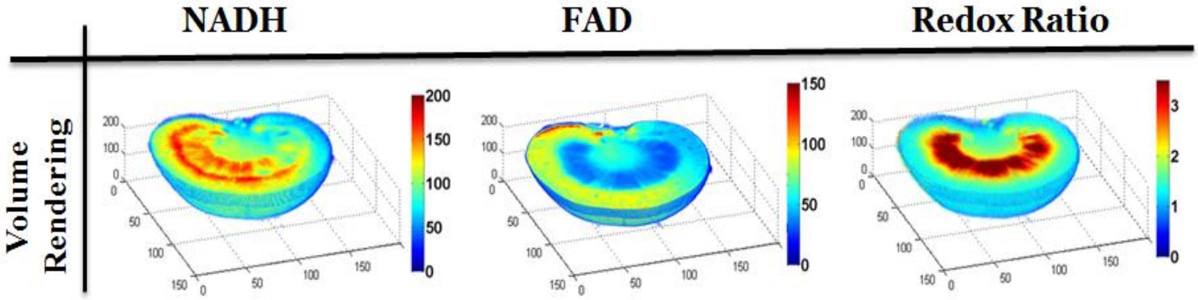

Figure 3-12: Volume rendering representative panel

The advantage of the whole volume method is that all of the voxels that belong to the tissue are involved in calculations of redox ratio. Therefore, it is a more precise method for the comparison of results between different groups.

In each injury model of my research, the more sensitive technique in terms of expected results has been selected to examine the NADH RR, and present the results. This issue has been discussed in chapter four in more detail.

3.4 Statistical analysis

All of the values are reported as mean ± standard error of the mean (SEM), where n refers to the number of rats used. Statistical significance ($p < 0.05$) was found based on two-tailed unpaired Student's t-test for each group of kidneys. In some of the studies, a two-way ANOVA followed by a Holm-Sidak post hoc test for multiple comparisons was used and significance determined at the $p<0.05$ level.

Chapter 4: Optical imaging of biological tissue

Overview

As a disease progresses, many changes occur within the body, including the alteration of organ structures and biochemical properties, the latter can result in the mitochondrial redox state. In order to study the effect of structural changes on the redox ratio, we study the correlation between changing vasculature structure in the kidneys and redox measurements in the hereditary hemorrhagic telangiectasia (HHT-1) disease model as well as gene knockout animal models. HHT-1 is used as a model to investigate the effects of disease on vasculature network in different organs. Hypertension can trigger excess generation of ROS and plays an important role in increasing OS, including kidneys. As we described earlier, there are several genomes that contribute to the development and progression of salt sensitive hypertension.

In this thesis, four categories of rats with different genotypes were used for hypertension studies. SS rats, which are the Dahl salt-sensitive rats have been used as a control model to compare with other three groups of rats. SS rats are more susceptible to OS and are thus expected to have a lower NADH RR. Other three groups (SSBN13, the NOX4$^{-/-}$, and the p67phox$^{-/-}$) are genetically modified Dahl salt-sensitive rats, which are protected against OS. Thus, they are compared to SS rats, and expected to have a higher NADH RR.

4.1 Cryo-Microscopy imaging: Endoglin (HHT-1 model)

HHT-1 is a dominant vascular dysplasia caused by loss-of-function mutations in the human Endoglin gene. HHT-1 results in excessive bleeding and vascular malformation due to failure to recruit perivascular supporting cells to the newly forming blood vessels [106]. Symptoms of HHT-1 include frequent nose bleeds, telangiectases, mucosa, and arteriovenous malformations in lung, liver, kidney, and brain [106, 107].

Complete deletion of the Endoglin gene is embryonically lethal. In mice with Endoglin gene knockout (Eng -/-), death occurs in utero from improper remodeling of their mature vascular network, leading to defects in the cardiovascular system. [11, 107-109].

In mice with partial knockout of the Endoglin gene (Eng +/-), vasculature was analyzed using the cryo-microscopy setup. Some observed vascular defects were consistent with those of Endoglin haploinsufficiency in humans [110]. Continuing to study vasculature as a result of structural changes allows the discovery of unknown aspects of the disease, which would prove useful in diagnosis and quantifying the severity of the organ injury due to this disease.

Figure 4-1 shows an Endoglin knockout mouse (Eng +/-) kidney versus that of a wild type mouse (Eng +/+), both sacrificed at nine months of age. The figure shows a maximum projection representation of the fluorescence signals of NADH and FAD, as well as the NADH redox ratio. In comparison to the wildtype mouse, the Endoglin knockout mouse shows an increased NADH signal and decreased FAD signal, and as a result, an increase in the NADH redox ratio. Figure 4-2 shows histograms of the NADH redox ratios of both the Eng +/- and Eng +/+ kidneys. The mean values of these histograms suggest a more oxidized mitochondrial redox state for the Eng +/- kidney, and a more reduced mitochondrial redox state for Eng +/+.

Figure 4-3 and Figure 4-4 show 3D renderings of the Eng +/- and Eng +/+ mouse kidneys

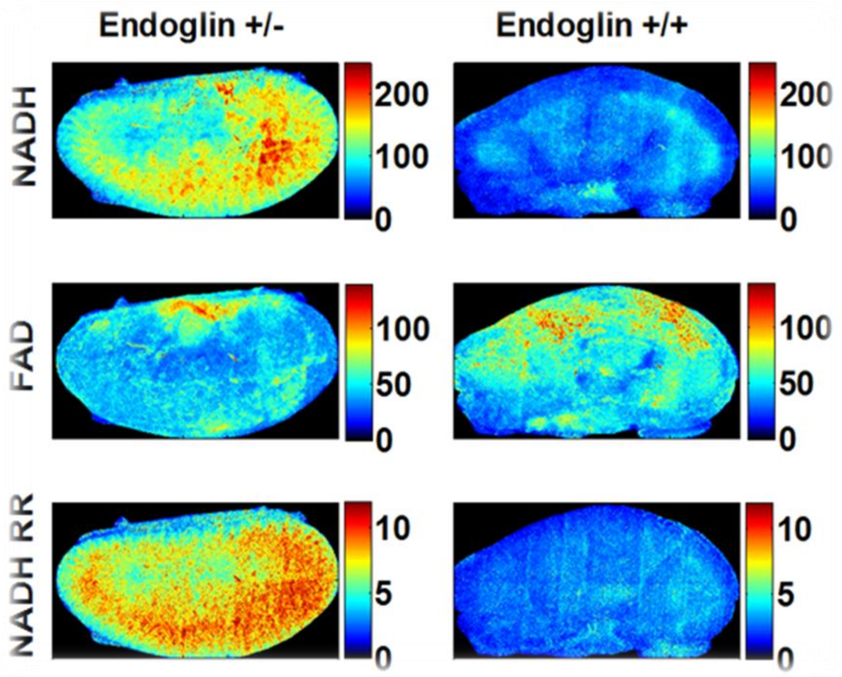

Figure 4-1: Maximum projection of NADH, FAD and NADH redox in 9 month Eng +/- and Eng +/+ mouse kidney

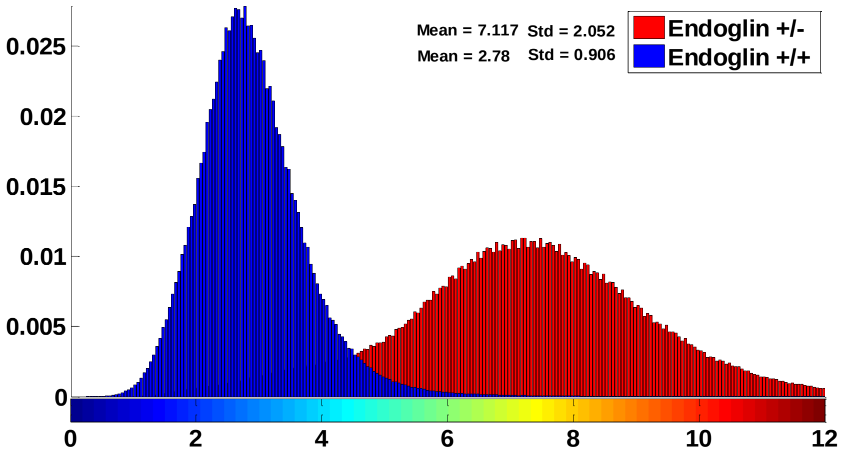

Figure 4-2: Histogram of NADH redox in 9 month Eng +/- (blue) and Eng +/+ (red) mouse kidney.

imaged in microscopy configuration. The automated edge detection algorithm has been applied to remove the background of the 2D slices, and preparing the nice 3D rendered. The comparison of these images illustrates more branching with smaller caliber and vessel coverage in the vasculature network of the Eng +/- kidney. These vessels are more torturous than those of the Eng +/+ kidney and demonstrate premature branching.

According to the comparison of the images, many properties exist, including amount of branching, size of caliber, amount of vessel coverage, premature branching, and tortuosity, that differ in the vasculature networks of kidneys in Eng +/- and Eng +/+ mice, as revealed by optical imaging using 3D cryo-microscopy.

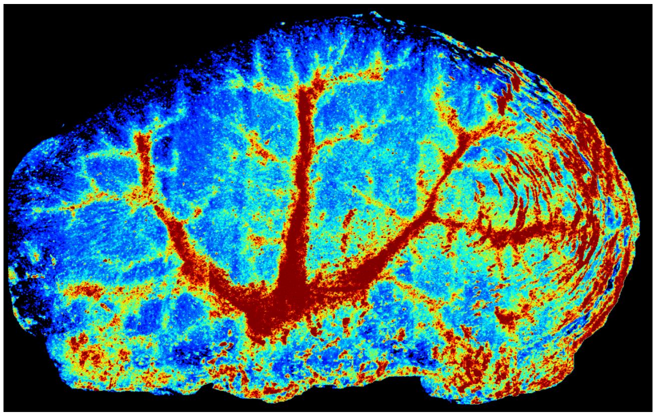

Figure 4-3: 3D rendering of NADH redox in 9 month Eng +/+ mouse kidney

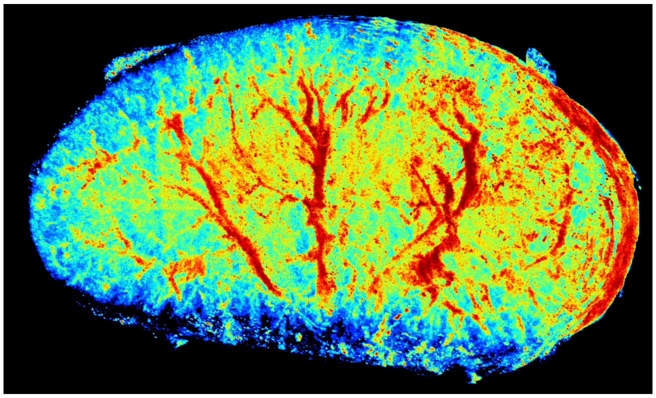

Figure 4-4: 3D rendering of NADH redox in 9 month Eng +/- mouse kidney sample.

4.2 Cryo-Macroscopy imaging: Hypertensive animal models

4.2.1 Tissue preparation (rodent model)

The following four groups of animals that have been used in this study:

SS rat: This strain is the Dahl salt-sensitive rat and is the control salt-sensitive strain used for the comparison to the SSBN13, the NOX4$^{-/-}$, and the p67phox$^{-/-}$.

SSBN13 rat: This strain is a salt-resistant consomic strain with the Brown Norway (BN) chromosome 13 introgressed into the Dahl salt-sensitive (SS) background [90].

NOX4$^{-/-}$ rat: This strain is the homozygous knockout of the NOX4 gene on the SS background achieved using zinc finger nuclease (ZFN) technology.

p67phox$^{-/-}$ rat: This strain is the homozygous knockout of the p67phox gene on the SS background using ZFN [7].

Diet protocol

Rats were fed a custom AIN-76 diet (Dyets, Inc., Bethlehem, PA) containing 0.4% NaCl , low salt (LS), since weaning. At 6 weeks of age, a subgroup of these rats was switched to a diet with 10-fold higher salt content, 4.0% NaCl diet (HS), for 21 days before the kidneys were collected.

On the day of tissue harvest, rats were deeply anesthetized with sodium pentobarbital (60mg/kg) and a catheter placed in the aorta for a rapid infusion of 20 ml of cold isotonic saline to flush the kidneys of blood. The left kidney was then quickly removed, hemisected, and rapidly frozen through specific protocol.

4.2.2 SS rats versus SSBN13 rats

Figure 4-5, is a representative panel of kidney fluorescent images to compare SS and SSBN13 rats. From top to bottom display the maximum intensity projected NADH, FAD, redox ratio, and its respective histogram are displayed, from SS and SSBN13 rats. The right graph shows the histogram of NADH RR of two group of rats. As the figure 4-5 shows, NADH signal of kidney from SSBN13 group is higher than SS kidneys. Differences in NADH RR images suggest that SSBN13 kidneys have a more reduced NADH respiratory chain than SS kidneys. Therefore, the NADH RR increased in renal medulla. The mean values of these histograms suggest a more reduced mitochondrial redox state for SSBN13 kidney compared to SS kidney.

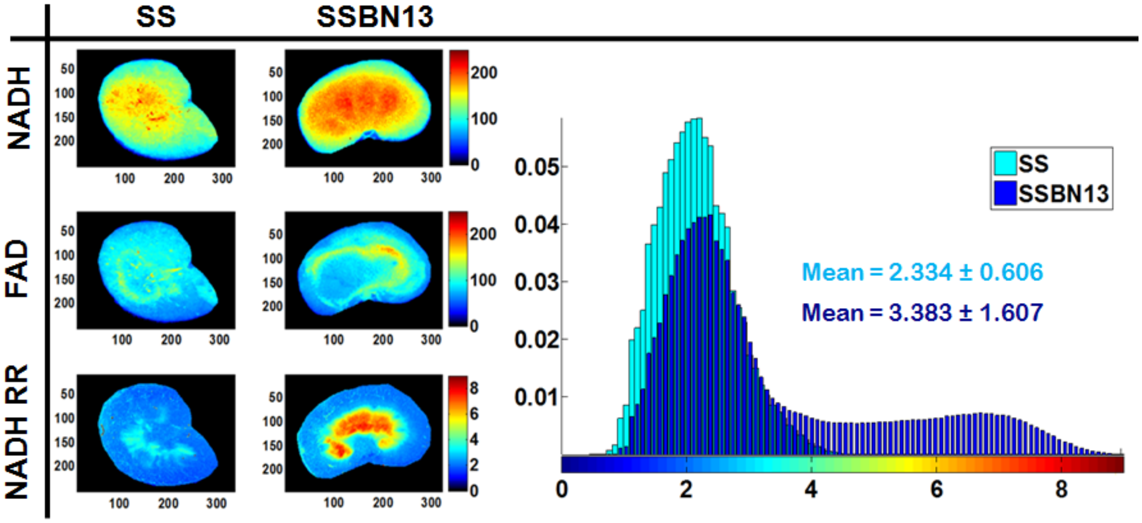

Figure 4-5:Maximum projection panel SS Vs. SSBN13 representative panel. Maximum intensity projected images of NADH (top), FAD (middle) and NADH RR (bottom) in salt-sensitive SS (left), SSBN13 (right) rat kidneys. Histogram distribution of NADH RR with their respective mean values.

Figure 4-6 displays a bar graph comparing the mean values of NADH RR from SSBN13 consomic strains versus SS rats. The results demonstrate a significant 49% decrease in the mean value of NADH RR in kidneys from a SS rat (2.143 ± 0.220; n=4) compared to a SSBN13 rat (3.189 ± 0.424; n=2) using student's t-test, with $P < 0.05$ as the criterion for statistical significance.

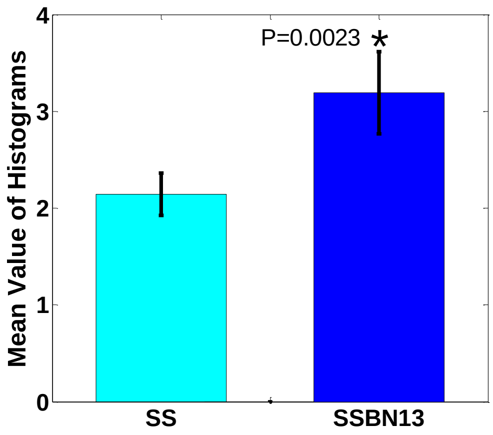

Figure 4-6: Statistical analysis SS versus SSBN13 rats. Bar graph showing the average values and standard errors of the mean value of the histogram of the mitochondrial redox ratio for each groups.

The renal medulla is the main region of interest to study the effect of chromosome 13 on tissue metabolism. To quantify regional injury, the middle slice of the representative kidney, which contains the largest portion of tissue, was selected to study the metabolic state of outer medulla. The NADH redox of the middle slice of representative kidneys, from both group of SS and SSBN13 rats, were measured and their corresponding histograms were plotted. Figure 4-7 (a) shows the middle slice from a representative kidney, from both groups of SS and SSBN13, and its respective histogram. The mean values of histograms were also calculated and presented. The result shows a

48% decrease in NADH RR. In figure 4-7 (b), a manually segmented medulla regions are selected and normalized histogram were obtained. By calculating the mean value of segmented regions, demonstrated in figure 4-7 (b), a 161% reduction of NADH RR occurred in SSBN13 kidney compared to SS. We conclude that this huge difference in percentage change is due the regional injury, which is mainly observed in renal medulla [92].

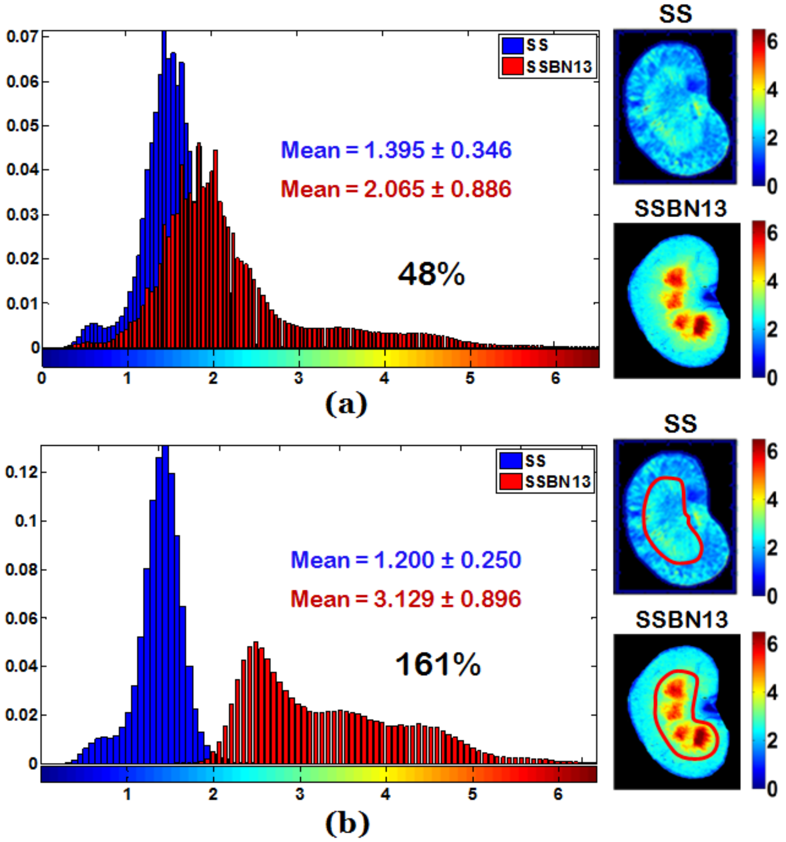

Figure 4-7: Percentage change of whole slice Vs. segmented medulla. (a) 2D images of the middle slice NADH redox of kidneys and their respective histograms and mean values**.(b)** 2D images of the largest slice NADH redox with segmented medulla of kidneys and the respective histogram of segmented part and mean values.

4.2.3 SS rats versus SS^{p67phox} null rats

Representative examples of 3-D images of the FAD and NADH fluorescence signals and their redox ratios (NADH RR = NADH/FAD) obtained from a representative SS rat and a SSp67phox null rat on 0.4% NaCl diet and a rat of each strain on 4.0% NaCl diet are shown in Figure 4-8. As can be seen, higher NADH and lower FAD fluorescence signals were observed within the renal medulla region of SSp67phox null rats compared to SS rats fed 0.4% NaCl diet. When fed 4.0% NaCl diet for 21 days, both strains of rats exhibited relatively higher levels of NADH RR throughout the kidney and especially in the renal medulla as apparent by the pseudo-red color intensity. Notably, the SSp67phox rat remained relatively well-protected from the high salt-induced oxidative stress as reflected by the high mitochondrial NADH RR values (higher NADH relative FAD) compared to the SS rat. These results indicate greater electron transport chain metabolic activity and reduction of oxidative stress in the renal medulla of the SSp67phox null mutant rats.

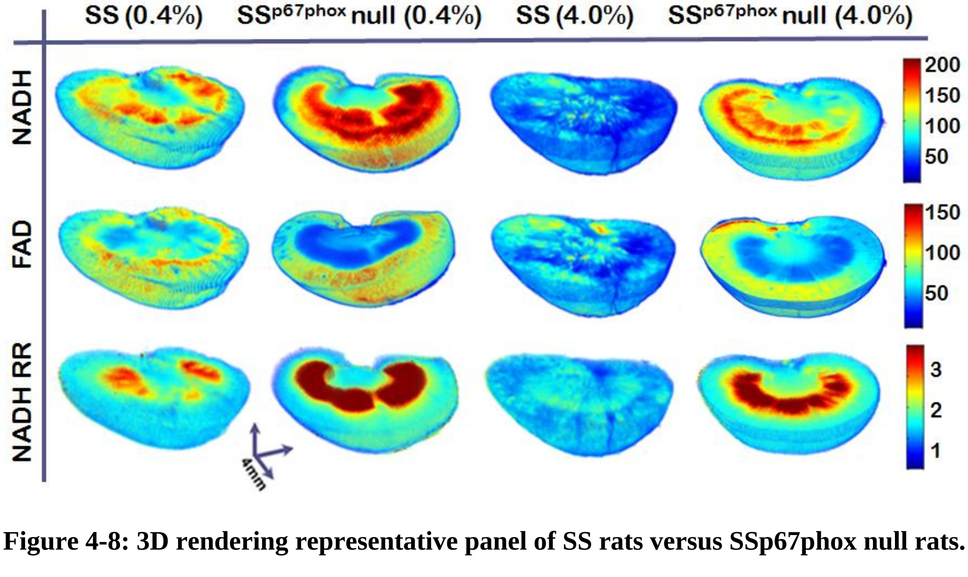

Figure 4-8: 3D rendering representative panel of SS rats versus SSp67phox null rats.

Figure 4-9 shows the corresponding histogram plots of NADH RR of the same four kidneys shown in Figure 4-8 in order to display the 3D fluorescence intensity distribution throughout the kidney tissue. The computed mean values of the normalized histograms (see Methods) clearly show that mitochondrial redox state is reduced in both SSp67phox null and SS rats in response to a high salt diet. However, SSp67phox null rat kidneys exhibited a lower overall level of oxidative stress throughout all regions.

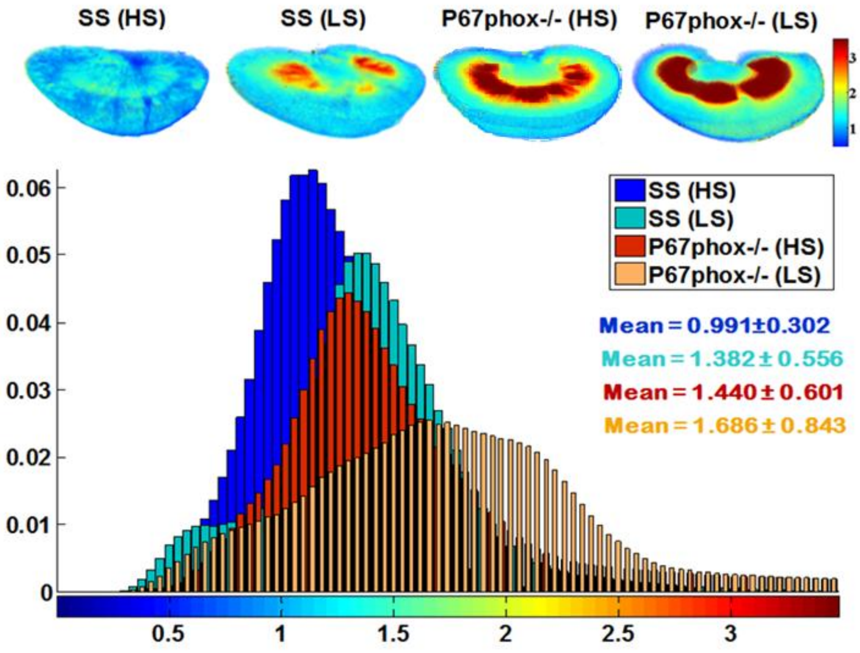

Figure 4-9: NADH Redox ratio histograms of representative kidneys.

Using this analysis method for all of the kidneys collected, Figure 4-10 summarizes the group data for the two strains on the two salt diets. The kidneys from the SS rats fed a 4.0% high salt diet (n=5) averaged a 43% decrease ($p<0.0005$) in the mean histogram of NADH Redox Ratio (RR) compared to kidneys from SS rats maintained on 0.4% NaCl diet (n=5), a consequence of a substantial reduction of NADH relative to FAD fluorescence. In contrast, the mean NADH RR of kidneys from the SSp67phox null rats (n=7) fed the 4.0% NaCl diet was reduced by only 14% when comparing kidneys from 0.4% NaCl fed rats (n=5). Even though high salt diet increased the mean NADH RR of SSp67phox null rats, this ratio was never greater than that observed in SS on 0.4% NaCl diet.

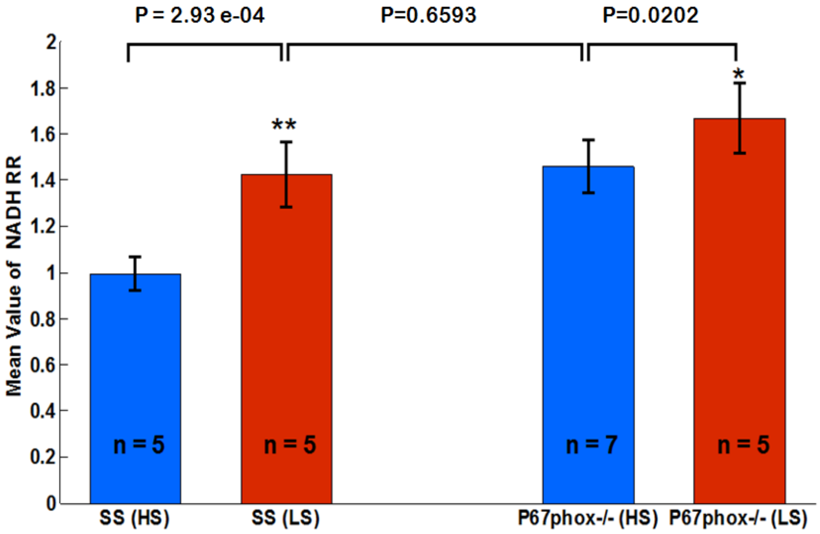

Figure 4-10: Statistical analysis SS versus SSp67phox null rats.

4.2.4 SS rats versus SS^{Nox4} null rats

To determine the effect of salt intake and Nox4 gene on the NADH RR, the mitochondrial redox state was determined on kidney from SS rats and SSNox4-/- rats fed on a 4.0% NaCl (HS) and 0.4% NaCl (LS) diet. Figure 4-11 displays the 3D rendering of FAD and NADH fluorescence signals, and their redox ratio (NADH RR) from representative kidneys of the four group of rats.

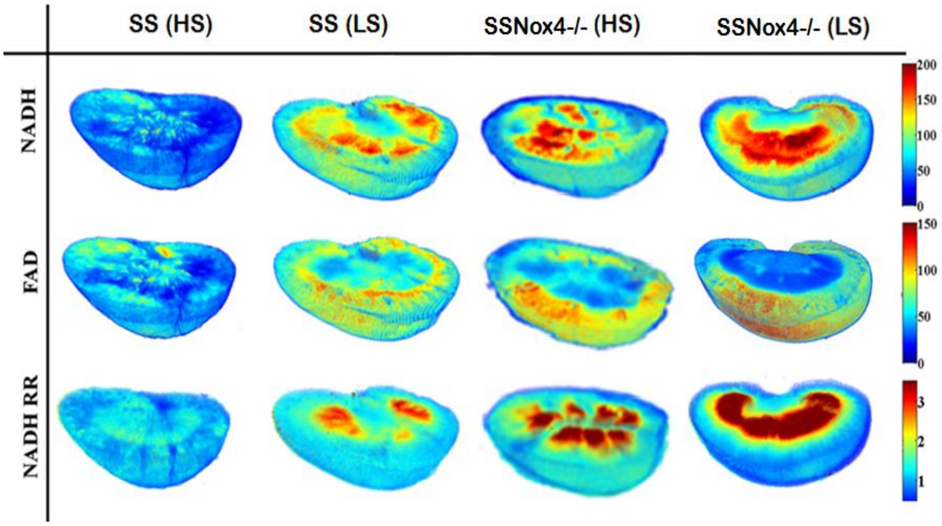

Figure 4-11: rendering representative panel of SS rats versus SSNox4 null rats.

As expected, less expression of Nox4 increases the NADH signal, and decreases the FAD in Medulla. Therefore, the NADH RR increased in renal medulla of SSNax4-/- groups compared to the SS groups. In the rats fed on HS diet, NADH RR shows a remarkable decease in comparison with LS diet kidneys. Figure 4-12 shows corresponding histograms of NADH RR of kidneys shown in representative panel (Fig. 4-11) to better compare the intensity distribution of the redox ratio. The mean values of the normalized histograms were calculated as described in image processing section. The mean values of these histograms suggest a more reduced mitochondrial redox state for knocked out (SSNox4-/-) kidneys compared to SS kidneys. There is a blue shift in histograms from LS diet versus HS diet kidneys. The tail of histograms is due to higher redox ratio in medulla region of kidneys.

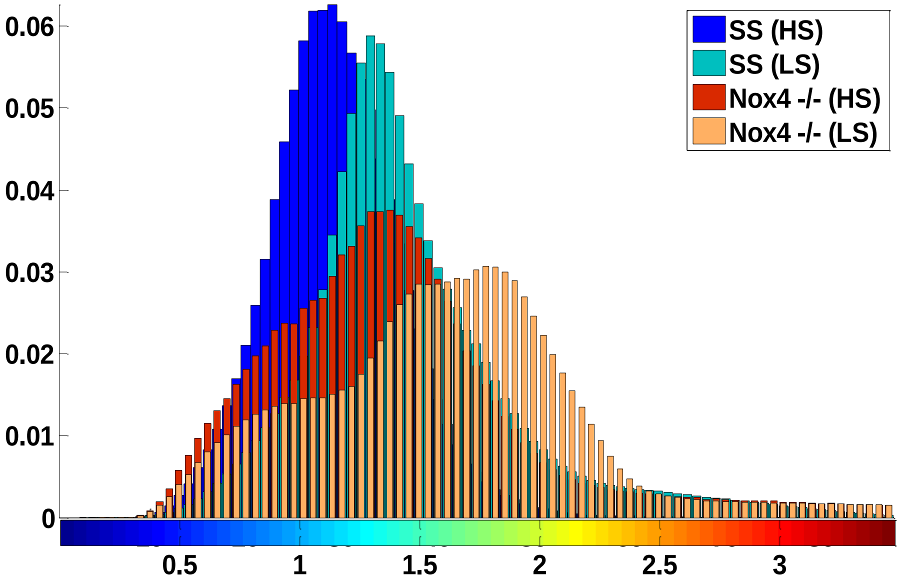

Figure 4-12: NADH Redox ratio histograms of representative kidneys.

To evaluate the statistical significance of the results, five kidneys in the SS groups (LS and HS), five kidneys in SSNox4-/- (LS) groups, and nine kidneys in SSNox4-/- (HS) groups were imaged. The mean values of the histograms of 3D rendered images were compared, the result of which is represented in figure 4-13. This figure displays a bar graph comparing the mean values of the histograms of 3D rendered images of kidneys from knocked out strains (SSNox4-/-) versus SS on both diet. The results demonstrate a remarkable 38% decrease ($p<0.0005$) in the mean histogram of NADH RR in kidneys from a SS rat on HS diet (0.994 ± 0.071; n=5) compared to a SS rat on LS diet

(1.425 ± 0.142; n=5). The result presented in the bar graph indicated that the mean NADH RR of kidney from knocked out strain (SSNox4-/-) on HS diet (1.384 ± 0.141; n=9) showed significant 18% decrease (P<0.05) in comparison with this stain on LS diet (1.639 ± 0.163; n=5). However, as Figure 4-13 shows kidneys from SS rats on LS diet exhibit a slight difference (0.5%) compared to the SSNox4-/- rats on HS diet. The direct effect of Nox4 gene in salt-induced hypertension and renal injury has not been explored in low salt diet, however the cryoimaging result can clearly show the protective effect of Nox4 gene on ROS production.

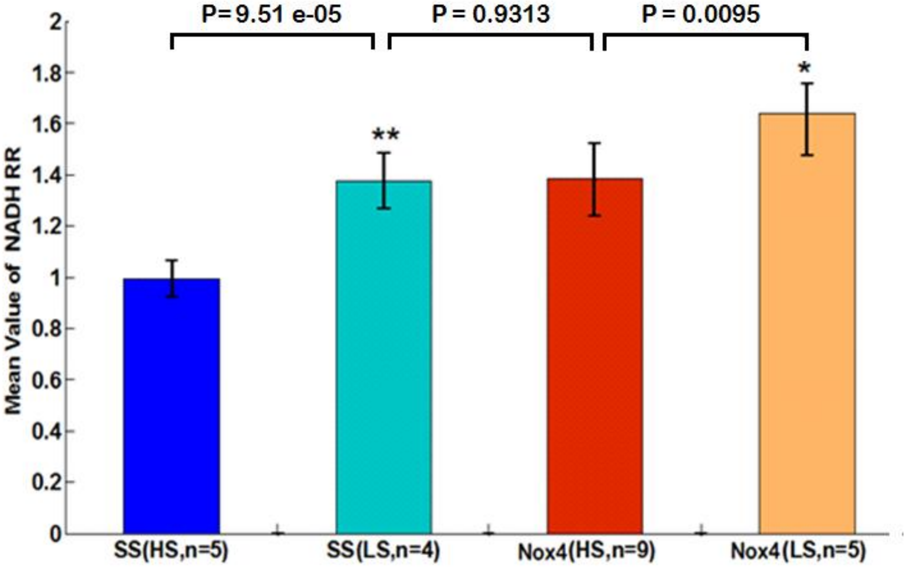

Figure 4-13: Statistical analysis SS versus SSNox4 null rats.

As we ascribed earlier, NADH and FADH2 are fluorescent when they are in their reduced and oxidized form, respectively. Therefore, the observed (fig.4-11) higher signal in NADH, and lower signal in FAD in SSNox4-/- rats is consistent with the fact that in the absence of Nox4 the mitochondrial coenzymes NADH and FAD accumulate in their reduced forms, so the chain become reduce. As a result, the mitochondrial NADH RR increase is associated to a decrease in oxidative stress. Figure 4-12 indicates 3D rendered of representative kidney of four groups, the SSNox4-/- on LS diet shows the highest NADH RR which is the representative of lowest ROS production, and it goes down as we move from right to the left. The lowest NADH RR is for SS high salt which is representative of highest ROS production, and the two middle one are not significantly different, statistically. It means that their NADH RR is almost in the same range, and the ROS production in these two groups is approximately the same. In the presence of excessive Nox4, renal damage occurred more rapidly, translated to a further decrease in NADH RR compared to its knocked out counterpart (Figure 4-13) and enhanced renal injuries. Thus, NADH RR can be used as a quantitative marker to evaluate the oxidative stress in knocked out genes in kidneys. The results revealed that salt-sensitive hypertension decreases the NADH RR in the kidney due to mitochondrial dysfunction, which is detectable by optical imaging. The 3D images also conclusively suggested that the increased oxidative stress in SS rats emanate almost entirely from the renal medulla.

Chapter 5: Conclusion and future work

5.1 Conclusion

In this research, I have improved upon an optical imaging instrument called the cryoimager to acquire 3D images of biological tissues in high resolution. I have also developed an algorithm written in MATLAB in order to improve the image processing. I have employed two different configurations of the cryo imager to study two different injury models.

In order to improve the quality of images taken by the cryo imaging system, I have optimized the slicing hardware to increase the smoothness of the slice surface. Furthermore, in order to achieve high resolution images, I extended the operation of the cryo imager from the macroscopic to the microscopic levels. This improvement has been done by upgrading the imaging setup and adding a raster scanning mechanism to capture high resolution and magnified images.

In addition, I have developed a fast image processing algorithm to automatically detect the tissue's boundary and remove the background from outside the detected borders. This algorithm has mostly been used in processing of high resolution imaging data. An improvement in the data analysis outcome has resulted from using this algorithm in a special case where we had problems with the mounting medium and low contrast images.

Using the 3D cryo-macroscopy setup, I have investigated protection against salt-sensitive hypertension associated with alterations of regional (mitochondrial) metabolism and oxidative stress within the kidney. For this study, the cryoimager enabled the direct assessment of the contribution of a selected gene on renal oxidative stress in SS rats.

The results show that even SS rats that were fed the non-hypertensive salt (0.4% NaCl) exhibit a lower mean NADH/FAD RR, indicating greater levels of oxidative stress compared to genetically manipulated rat kidneys (SSBN13, SSp67pho-/- ,SSNox4-/-). It is evident from the results that the major differences in oxidative stress were observed most prominently in the renal medullary region of the kidney, which is rich in mitochondria, signifying the involvement of mitochondria in oxidative stress. This difference in redox ratio between the SS and genetically modified rats substantially increased as a consequence of high salt (4.0% NaCl) feeding. Importantly, this data indicates that genetically-altered rat kidneys remain relatively well protected from oxidative stress.

Using the implemented 3D cryo-microscopy setup, I investigated simultaneous examination of the tissue redox state and the structural deformation in the vasculature network of mouse kidneys caused by HHT-1. HHT-1 (Hereditary hemorrhagic telangiectasia) is our disease model. The results showed that in the absence of the endoglin gene, the vasculature network in the kidney has more branching, is smaller caliber, has smaller vessel coverage, and has premature branching in respect to control mice. The Endoglin knockout mouse also showed higher NADH RR, which translates to more oxidized mitochondrial redox state.

I conclude from the present study that optical fluorescence 3D cryoimaging can effectively assess the effects of genetic manipulation on renal function and dysfunction. The optical cryoimaging technique including two different macroscopic and microscopic configurations provides a useful tool for the analysis of the cellular redox states of the kidney, as well as structural changes in various disease models.

5.2 Future work

The capabilities of the cryoimaging system are essential for 3D imaging of biological studies. This system could be improved in the future by enhancement of high resolution imaging at cellular and sub-cellular resolutions. In terms of instrumentation, the next step to improve the following generation of the cryoimaging system would be to add an active optical table to separate the optical components from mechanical part of the instrument. In this way, the vibrations caused by the freezer's compressor will not affect the quality of the image acquisition in the high resolution imaging setup. We can also design a more robust enclosure for the optical components in order to eliminate the ambient lights.

In terms of image processing, a productive step would be to extend the automated segmentation algorithm to 3D using active contour method to quantify regional injury in salt sensitive kidneys. An image processing algorithm should be developed to quantify the variation of vessel coverage due to injuries such as HHT-1. In addition, the Nox4 gene is highly expressed within the endothelium and contributes to ROS production. It has been shown that endogenous Nox4 protects the vasculature during ischemic or inflammatory stress [47, 111]. The future direction could be to use a cryomicroscopy setup to evaluate the protective vascular function of Nox4 in the kidneys at higher resolutions.

REFRENCES

[1] (4/1/2015). *Biophotonics*. Available: http://www.conferenceseries.com/biophotonics.php

[2] T. M. C. SALEH Bahaa E. A., *Fundamentals of photonics* 2nd ed. New York: JOHN WILEY 2009.

[3] T. Vo-Dinh, *Biomedical photonics handbook*. Boca Raton: CRC Press, 2003.

[4] V. Tuchin, *Tissue Optics: Light Scattering Methods and Instruments for Medical Diagnosis*, 2nd ed. vol. PM166: SPIE Press Monograph, 2007.

[5] G. A. Wagnieres, *et al.*, "In vivo fluorescence spectroscopy and imaging for oncological applications," *Photochem Photobiol,* vol. 68, pp. 603-32, Nov 1998.

[6] M. Olivo*, et al.*, "Advances in fluorescence diagnosis to track footprints of cancer progression in vivo," *Laser & Photonics Reviews,* vol. 7, pp. 646-662, Sep 2013.

[7] D. Feng*, et al.*, "Increased expression of NAD(P)H oxidase subunit p67(phox) in the renal medulla contributes to excess oxidative stress and salt-sensitive hypertension," *Cell Metab,* vol. 15, pp. 201-8, Feb 8 2012.

[8] G. Danaei*, et al.*, "National, regional, and global trends in systolic blood pressure since 1980: systematic analysis of health examination surveys and epidemiological studies with 786 country-years and 5.4 million participants," *Lancet,* vol. 377, pp. 568-77, Feb 12 2011.

[9] P. M. Kearney*, et al.*, "Global burden of hypertension: analysis of worldwide data," *Lancet,* vol. 365, pp. 217-23, Jan 15-21 2005.

[10] C. Kitiyakara*, et al.*, "Salt intake, oxidative stress, and renal expression of NADPH oxidase and superoxide dismutase," *J Am Soc Nephrol,* vol. 14, pp. 2775-82, Nov 2003.

[11] D. Y. Li*, et al.*, "Defective angiogenesis in mice lacking endoglin," *Science,* vol. 284, pp. 1534-7, May 28 1999.

[12] K. A. McAllister*, et al.*, "Endoglin, a TGF-beta binding protein of endothelial cells, is the gene for hereditary haemorrhagic telangiectasia type 1," *Nat Genet,* vol. 8, pp. 345-51, Dec 1994.

[13] S. Park*, et al.*, "Endoglin Regulates the Activation and Quiescence of Endothelium by Participating in Canonical and Non-Canonical TGF-beta Signaling Pathways," *J Cell Sci,* Feb 15 2013.

[14] B. Alberts, *Molecular biology of the cell*, 4th ed. New York: Garland Science, 2002.

[15] (4/2/2015). *Biological_cell*. Available: http://upload.wikimedia.org/wikipedia/commons/thumb/e/e0/Biological_cell_vacuole.svg/1466px-Biological_cell_vacuole.svg.png

[16] E. N. Marieb and K. Hoehn, *Human anatomy & physiology*, 8th ed. San Francisco: Benjamin Cummings, 2010.

[17] M. W. Davidson. (2015, 2/4/2015). *Mitochondria*. Available: http://micro.magnet.fsu.edu/cells/mitochondria/mitochondria.html

[18] K. Henze and W. Martin, "Evolutionary biology: essence of mitochondria," *Nature,* vol. 426, pp. 127-8, Nov 13 2003.

[19] D. Voet, *et al.*, *Fundamentals of biochemistry : life at the molecular level*, 2nd ed. Hoboken, N.J.: Wiley, 2006.

[20] F. A. Villamena, *Molecular Basis of Oxidative Stress: Chemistry, Mechanisms, and Disease Pathogenesis*. Columbos, Ohio: Wiley, 2013.

[21] N. A. Campbell, *et al.*, *Biology: Exploring Life*. Boston, Massachusetts: Pearson Prentice Hall, 2006.

[22] (4/2/2015). *Electron Transport Chain*. Available: http://sciencesoup.tumblr.com/post/92192632459/electron-transport-chain-from-the-mitochondrial

[23] K. Staniszewski*, et al.*, "Surface fluorescence studies of tissue mitochondrial redox state in isolated perfused rat lungs," *Ann Biomed Eng,* vol. 41, pp. 827-36, Apr 2013.

[24] A. Mayevsky and G. G. Rogatsky, "Mitochondrial function in vivo evaluated by NADH fluorescence: from animal models to human studies," *American Journal of Physiology-Cell Physiology,* vol. 292, pp. C615-C640, Feb 2007.

[25] B. Chance and H. Baltscheffsky, "Respiratory enzymes in oxidative phosphorylation. VII. Binding of intramitochondrial reduced pyridine nucleotide," *J Biol Chem,* vol. 233, pp. 736-9, Sep 1958.

[26] B. Chance*, et al.*, "Intracellular Oxidation-Reduction States in Vivo," *Science,* vol. 137, pp. 499-508, 17 August 1962 1962.

[27] A. A. Heikal, "Intracellular coenzymes as natural biomarkers for metabolic activities and mitochondrial anomalies," *Biomarkers in Medicine,* vol. 4, pp. 241-263, Apr 2010.

[28] R. Scholz*, et al.*, "Flavin and pyridine nucleotide oxidation-reduction changes in perfused rat liver. I. Anoxia and subcellular localization of fluorescent flavoproteins," *J Biol Chem,* vol. 244, pp. 2317-24, May 10 1969.

[29] M. Aldakkak*, et al.*, "Modulation of mitochondrial bioenergetics in the isolated Guinea pig beating heart by potassium and lidocaine cardioplegia: implications for cardioprotection," *J Cardiovasc Pharmacol,* vol. 54, pp. 298-309, Oct 2009.

[30] J. R. Koke*, et al.*, "Sensitivity of flavoprotein fluorescence to oxidative state in single isolated heart cells," *Cytobios,* vol. 32, pp. 139-45, 1981.

[31] J. M. Mates and F. M. Sanchez-Jimenez, "Role of reactive oxygen species in apoptosis: implications for cancer therapy," *Int J Biochem Cell Biol,* vol. 32, pp. 157-70, Feb 2000.

[32] B. Halliwell and J. M. C. Gutteridge, *Free radicals in biology and medicine* vol. 4th ed. New York: Oxford University Press, 2007.

[33] R. M. Touyz, "Reactive oxygen species, vascular oxidative stress, and redox signaling in hypertension: what is the clinical significance?," *Hypertension,* vol. 44, pp. 248-52, Sep 2004.

[34] T. M. Paravicini and R. M. Touyz, "NADPH oxidases, reactive oxygen species, and hypertension: clinical implications and therapeutic possibilities," *Diabetes Care,* vol. 31 Suppl 2, pp. S170-80, Feb 2008.

[35] K. Staniszewski, "OPTICAL INSTRUMENTATION AND IMAGE CYTOMETRY OF LUNG AND EYE INJURIES: STUDIES IN THE RODENT MODEL," Master, Electrical Engineering, University of Wisconsin-Milwaukee, Milwaukee, 2012.

[36] B. M. Babior, "NADPH oxidase: an update," *Blood,* vol. 93, pp. 1464-76, Mar 1 1999.

[37] B. Lassegue and K. K. Griendling, "NADPH oxidases: functions and pathologies in the vasculature," *Arterioscler Thromb Vasc Biol,* vol. 30, pp. 653-61, Apr 2010.

[38] B. M. Babior, "NADPH oxidase," *Curr Opin Immunol,* vol. 16, pp. 42-7, Feb 2004.

[39] T. Chabrashvili, *et al.*, "Expression and cellular localization of classic NADPH oxidase subunits in the spontaneously hypertensive rat kidney," *Hypertension,* vol. 39, pp. 269-74, Feb 2002.

[40] K. Bedard and K. H. Krause, "The NOX family of ROS-generating NADPH oxidases: physiology and pathophysiology," *Physiol Rev,* vol. 87, pp. 245-313, Jan 2007.

[41] K. Lapouge, *et al.*, "Structure of the TPR domain of p67phox in complex with Rac.GTP," *Mol Cell,* vol. 6, pp. 899-907, Oct 2000.

[42] T. L. Leto and M. Geiszt, "Role of Nox family NADPH oxidases in host defense," *Antioxid Redox Signal,* vol. 8, pp. 1549-61, Sep-Oct 2006.

[43] M. Geiszt, "NADPH oxidases: new kids on the block," *Cardiovasc Res,* vol. 71, pp. 289-99, Jul 15 2006.

[44] A. C. Cave, *et al.*, "NADPH oxidases in cardiovascular health and disease," *Antioxid Redox Signal,* vol. 8, pp. 691-728, May-Jun 2006.

[45] K. K. Griendling, "NADPH oxidases: new regulators of old functions," *Antioxid Redox Signal,* vol. 8, pp. 1443-5, Sep-Oct 2006.

[46] M. Geiszt, *et al.*, "Identification of renox, an NAD(P)H oxidase in kidney," *Proc Natl Acad Sci U S A,* vol. 97, pp. 8010-4, Jul 5 2000.

[47] R. M. Touyz and A. C. Montezano, "Vascular Nox4: a multifarious NADPH oxidase," *Circ Res,* vol. 110, pp. 1159-61, Apr 27 2012.

[48] S. R. Datla and K. K. Griendling, "Reactive oxygen species, NADPH oxidases, and hypertension," *Hypertension,* vol. 56, pp. 325-30, Sep 2010.

[49] I. Diebold, *et al.*, "The NADPH oxidase subunit NOX4 is a new target gene of the hypoxia-inducible factor-1," *Mol Biol Cell,* vol. 21, pp. 2087-96, Jun 15 2010.

[50] J. G. Fujimoto, *et al.*, "Optical coherence tomography: an emerging technology for biomedical imaging and optical biopsy," *Neoplasia,* vol. 2, pp. 9-25, Jan-Apr 2000.

[51] D. A. Boas, *et al.*, *Handbook of biomedical optics*. Boca Raton: CRC Press, 2011.

[52] S. Andersson-Engels, *et al.*, "In vivo fluorescence imaging for tissue diagnostics," *Phys Med Biol,* vol. 42, pp. 815-24, May 1997.

[53] J. H. Markus Sauer, Jörg Enderlein, *Handbook of Fluorescence Spectroscopy and Imaging: From Single Molecules to Ensembles*: Wiley, 2011.

[54] Z. Ghanian, *et al.*, "Organ specific optical imaging of mitochondrial redox state in a rodent model of hereditary hemorrhagic telangiectasia-1," *J Biophotonics,* Jun 6 2013.

[55] R. Sepehr, *et al.*, "Optical imaging of tissue mitochondrial redox state in intact rat lungs in two models of pulmonary oxidative stress," *J Biomed Opt,* vol. 17, p. 046010, Apr 2012.

[56] S. Maleki, *et al.*, "Mitochondrial redox studies of oxidative stress in kidneys from diabetic mice," *Biomedical Optics Express,* vol. 3, pp. 273-81, Feb 1 2012.

[57] (4/3/2015). *Fluorescence Imaging*. Available: http://malone.bioquant.uni-heidelberg.de/methods/imaging/imaging.html

[58] L. V. Wang, "Biomedical Optics: Principles and Imaging," 06/04/2007 ed. Washington University: Wiley, 2007.

[59] J. M. Christie, *et al.*, "LOV (light, oxygen, or voltage) domains of the blue-light photoreceptor phototropin (nph1): Binding sites for the chromophore flavin mononucleotide," *Proceedings of the National Academy of Sciences of the United States of America,* vol. 96, pp. 8779-8783, Jul 20 1999.

[60] G. H. Patterson, *et al.*, "Separation of the glucose-stimulated cytoplasmic and mitochondrial NAD(P)H responses in pancreatic islet beta cells," *Proc Natl Acad Sci U S A,* vol. 97, pp. 5203-7, May 9 2000.

[61] B. Chance, *et al.*, "Oxidation-reduction ratio studies of mitochondria in freeze-trapped samples. NADH and flavoprotein fluorescence signals," *J Biol Chem,* vol. 254, pp. 4764-71, Jun 10 1979.

[62] Z. Ghanian, *et al.*, "Optical imaging of mitochondrial redox state in rodent models with 3-iodothyronamine," *Experimental Biology and Medicine,* vol. 239, pp. 151-158, Feb 2014.

[63] R. Sepehr, *et al.*, "Fluorescence Spectroscopy and Cryoimaging of Rat Lung Tissue Mitochondrial Redox State," in *SPIE,* Munich, 2011.

[64] (2015, 4/15/2015). *High Blood Pressure and Kidney Disease*. Available: http://www.medicinenet.com/kidney_disease_hypertension-related/article.htm

[65] A. Aviv, *et al.*, "Urinary potassium excretion and sodium sensitivity in blacks," *Hypertension,* vol. 43, pp. 707-13, Apr 2004.

[66] J. M. Sullivan, *et al.*, "Sodium sensitivity in normotensive and borderline hypertensive humans," *Am J Med Sci,* vol. 295, pp. 370-7, Apr 1988.

[67] M. H. Weinberger, "Salt sensitivity of blood pressure in humans," *Hypertension,* vol. 27, pp. 481-90, Mar 1996.

[68] R. J. Roman, "Abnormal renal hemodynamics and pressure-natriuresis relationship in Dahl salt-sensitive rats," *Am J Physiol,* vol. 251, pp. F57-65, Jul 1986.

[69] R. J. Roman and M. L. Kaldunski, "Enhanced chloride reabsorption in the loop of Henle in Dahl salt-sensitive rats," *Hypertension,* vol. 17, pp. 1018-24, Jun 1991.

[70] C. Kitiyakara, *et al.*, "Salt intake, oxidative stress, and renal expression of NADPH oxidase and superoxide dismutase," *Journal of the American Society of Nephrology,* vol. 14, pp. 2775-2782, Nov 2003.

[71] P. S. Gill and C. S. Wilcox, "NADPH oxidases in the kidney," *Antioxid Redox Signal,* vol. 8, pp. 1597-607, Sep-Oct 2006.

[72] P. D. Cabral, *et al.*, "Shear stress increases nitric oxide production in thick ascending limbs," *Am J Physiol Renal Physiol,* vol. 299, pp. F1185-92, Nov 2010.

[73] J. C. Jha, *et al.*, "Genetic targeting or pharmacologic inhibition of NADPH oxidase nox4 provides renoprotection in long-term diabetic nephropathy," *J Am Soc Nephrol,* vol. 25, pp. 1237-54, Jun 2014.

[74] R. J. Roman, *et al.*, "Renal P450 metabolites of arachidonic acid and the development of hypertension in Dahl salt-sensitive rats," *Am J Hypertens,* vol. 10, pp. 63S-67S, May 1997.

[75] P. N. Seshiah, *et al.*, "Angiotensin II stimulation of NAD(P)H oxidase activity: upstream mediators," *Circ Res,* vol. 91, pp. 406-13, Sep 6 2002.

[76] N. Kuzkaya, *et al.*, "Interactions of peroxynitrite, tetrahydrobiopterin, ascorbic acid, and thiols: implications for uncoupling endothelial nitric-oxide synthase," *J Biol Chem,* vol. 278, pp. 22546-54, Jun 20 2003.

[77] W. G. Li, *et al.*, "H(2)O(2)-induced O(2) production by a non-phagocytic NAD(P)H oxidase causes oxidant injury," *J Biol Chem,* vol. 276, pp. 29251-6, Aug 3 2001.

[78] J. S. McNally, *et al.*, "Regulation of xanthine oxidoreductase protein expression by hydrogen peroxide and calcium," *Arterioscler Thromb Vasc Biol,* vol. 25, pp. 1623-8, Aug 2005.

[79] R. Radi, *et al.*, "Peroxynitrite reactions and formation in mitochondria," *Free Radic Biol Med,* vol. 33, pp. 1451-64, Dec 1 2002.

[80] N. J. Hong and J. L. Garvin, "NADPH oxidase 4 mediates flow-induced superoxide production in thick ascending limbs," *Am J Physiol Renal Physiol,* vol. 303, pp. F1151-6, Oct 15 2012.

[81] N. E. Taylor, *et al.*, "NADPH oxidase in the renal medulla causes oxidative stress and contributes to salt-sensitive hypertension in Dahl S rats," *Hypertension,* vol. 47, pp. 692-8, Apr 2006.

[82] A. W. Cowley, Jr., "The genetic dissection of essential hypertension," *Nat Rev Genet,* vol. 7, pp. 829-40, Nov 2006.

[83] A. M. Geurts, *et al.*, "Maternal diet during gestation and lactation modifies the severity of salt-induced hypertension and renal injury in Dahl salt-sensitive rats," *Hypertension,* vol. 65, pp. 447-55, Feb 2015.

[84] T. A. Kotchen, *et al.*, "Salt in health and disease--a delicate balance," *N Engl J Med,* vol. 368, pp. 1229-37, Mar 28 2013.

[85] M. J. Flister, *et al.*, "Congenic mapping and sequence analysis of the Renin locus," *Hypertension,* vol. 61, pp. 850-6, Apr 2013.

[86] M. J. Flister, *et al.*, "Identifying multiple causative genes at a single GWAS locus," *Genome Res,* vol. 23, pp. 1996-2002, Dec 2013.

[87] M. J. Hoffman, *et al.*, "Female-specific hypertension loci on rat chromosome 13," *Hypertension,* vol. 62, pp. 557-63, Sep 2013.

[88] C. Moreno, *et al.*, "Multiple blood pressure loci on rat chromosome 13 attenuate development of hypertension in the Dahl S hypertensive rat," *Physiol Genomics,* vol. 31, pp. 228-35, Oct 22 2007.

[89] M. Stoll, *et al.*, "A genomic-systems biology map for cardiovascular function," *Science,* vol. 294, pp. 1723-6, Nov 23 2001.

[90] A. W. Cowley, Jr., *et al.*, "Brown Norway chromosome 13 confers protection from high salt to consomic Dahl S rat," *Hypertension,* vol. 37, pp. 456-61, Feb 2001.

[91] C. Moreno, *et al.*, "Narrowing a region on rat chromosome 13 that protects against hypertension in Dahl SS-13(BN) congenic strains," *American Journal of Physiology-Heart and Circulatory Physiology,* vol. 300, pp. H1530-H1535, Apr 2011.

[92] F. Salehpour, T. Kurth, A.W. Cowley, Jr, M. Ranji "Optical cryoimaging of rat kidney and effective role of chromosome 13 in salt-induced hypertension," *SPIE Proceedings*, vol. 9321, 5 March 2015.

[93] A. M. Geurts, *et al.*, "Knockout rats via embryo microinjection of zinc-finger nucleases," *Science,* vol. 325, p. 433, Jul 24 2009.

[94] A. M. Geurts, *et al.*, "Generation of gene-specific mutated rats using zinc-finger nucleases," *Methods Mol Biol,* vol. 597, pp. 211-25, 2010.

[95] Y. Maehara, *et al.*, "Role for the first SH3 domain of p67phox in activation of superoxide-producing NADPH oxidases," *Biochem Biophys Res Commun,* vol. 379, pp. 589-93, Feb 6 2009.

[96] D. Noack, *et al.*, "Autosomal recessive chronic granulomatous disease caused by novel mutations in NCF-2, the gene encoding the p67-phox component of phagocyte NADPH oxidase," *Hum Genet,* vol. 105, pp. 460-7, Nov 1999.

[97] M. W. Davidson. (2015, (4/24/2015)). *Education in Microscopy and Digital Imaging*. Available: http://zeiss-campus.magnet.fsu.edu/articles/lightsources/mercuryarc.html

[98] (4/15/2015). *Cold Mirror*. Available: http://www.edmundoptics.com/optics/optical-mirrors/specialty-mirrors/cold-mirrors/1900/

[99] (2015, 4/15/2015). *Rolera EM-C2 User’s Manual*. Available: http://www.qimaging.com/resources/pdfs/Rolera-EMC2-Manual.pdf

[100] (4/15/2015). *EF 28-135mm f/3.5-5.6 IS USM Standard Zoom*. Available: http://www.usa.canon.com/cusa/consumer/products/cameras/ef_lens_lineup/ef_28_135mm_f_3_5_5_6_is_usm

[101] (January 2014). *Optem Zoom 125C 12.5:1 Micro-Inspection Lens System*. Available: http://www.qioptiq.com/optem-micro-12-5.html

[102] J. L. Prince and J. M. Links, *Medical imaging signals and systems*. Upper Saddle River, NJ: Pearson Prentice Hall, 2006.

[103] (February 2014). *LENS QUALITY: MTF, RESOLUTION & CONTRAST*. Available: http://www.cambridgeincolour.com/tutorials/lens-quality-mtf-resolution.htm

[104] M. MasoudiMotlagh, "CRYOIMAGING-MICROSCOPY IMPLEMENTATION FOR 3D OPTICAL IMAGING," Master, Electrical engineering, University of Wisconsin-Milwaukee, Milwaukee, 2014.

[105] R. E. W. Rafael C. Gonzalez, in *Digital Image Processing*, 3rd ed: Addison-Wesley Pub 2007.

[106] K. A. Mcallister, *et al.*, "Endoglin, a Tgf-Beta Binding-Protein of Endothelial-Cells, Is the Gene for Hereditary Hemorrhagic Telangiectasia Type-1," *Nature Genetics*, vol. 8, pp. 345-351, Dec 1994.

[107] A. Alt, *et al.*, "Structural and Functional Insights into Endoglin Ligand Recognition and Binding," *Plos One*, vol. 7, Feb 8 2012.

[108] H. M. Arthur, *et al.*, "Endoglin, an ancillary TGFbeta receptor, is required for extraembryonic angiogenesis and plays a key role in heart development," *Dev Biol*, vol. 217, pp. 42-53, Jan 1 2000.

[109] A. Bourdeau, *et al.*, "A murine model of hereditary hemorrhagic telangiectasia," *J Clin Invest*, vol. 104, pp. 1343-51, Nov 1999.

[110] M. Mahmoud, *et al.*, "Pathogenesis of arteriovenous malformations in the absence of endoglin," *Circ Res*, vol. 106, pp. 1425-33, Apr 30 2010.

[111] K. Schroder, *et al.*, "Nox4 is a protective reactive oxygen species generating vascular NADPH oxidase," *Circ Res*, vol. 110, pp. 1217-25, Apr 27 2012.